Preprint

A machine learning-based thermometer, barometer and hygrometer for magmatic liquids

Gregor Weber[*1,2], Jon Blundy[1]

[1]Department of Earth Sciences, University of Oxford, OX1 3AN Oxford, United Kingdom

[2]School of Earth Sciences, University of Bristol, BS8 1RJ Bristol, United Kingdom

*Corresponding author (gregor.weber@bristol.ac.uk)

A machine learning-based thermometer, barometer and hygrometer for magmatic liquids

Gregor Weber*[1,2], Jon Blundy[1]
[1]Department of Earth Sciences, University of Oxford, OX1 3AN Oxford, United Kingdom
[2]School of Earth Sciences, University of Bristol, BS8 1RJ Bristol, United Kingdom
*Corresponding author (gregor.weber@bristol.ac.uk)

ABSTRACT

Experimentally calibrated models to recover pressures, temperatures and water contents of magmas, are widely used in igneous petrology. However, large errors, especially in barometry, limit the capacity of these models to resolve the architecture of crustal igneous systems. Here we apply machine learning to a large experimental database to calibrate new regression models that recover P-T-H_2O of magmas based on either melt composition or melt composition plus associated phase assemblage. The method is applicable to compositions from basalt to rhyolite, pressures from 0.2 to 14.5 kbar, temperatures of 675-1425°C, and H_2O contents up to 15 wt.%. Testing and optimisation of the model show that pressures can be recovered with root-mean-square-error (RMSE) of 1.2 and 1.0 kbar for the melt-only and melt-phase assemblage models respectively. Errors on temperature estimates are 22-25°C and 1.0-1.3 wt.% for H_2O. Our findings demonstrate that melt chemistry is a reliable recorder of magmatic variables. This is a consequence of the relatively low thermodynamic variance of natural magma compositions despite their relatively large number of constituent oxide components. We apply our model to three contrasting cases with well-constrained geophysical information: Mount St. Helens volcano in the Cascades arc (USA), the Altiplano-Puna Volcanic Complex (APVC) in Chile, and the Askja caldera in Iceland. Dacite whole-rocks from Mount St Helens erupted 1980-1986 yield magma source pressures of 3.3-4.3 kbar in excellent agreement with experimental petrology, seismic tomography, magnetotelluric images and earthquake hypocentres. Melt inclusions and matrix glasses record lower pressures, consistent with magma crystallisation during ascent. Glasses and phase assemblages for three large magnitude APVC eruptions (Atana, Toconao, Purico ignimbrites) yield magma storage pressures and temperatures of 1.7-2.4 kbar and 726-789°C, in excellent agreement with previous thermobarometry. While these pressures are shallower than the underlying Altiplano-Puna Magma Body (APMB), rhyolite whole-rock compositions indicate pressures equivalent to the top of the APMB. We suggest that extraction of rhyolitic liquids from the APMB mush, followed by crystallisation at shallower depth preceded each eruption. Magma reservoir depth estimates for historical eruptions from Askja match the location of seismic wave speed anomalies. We show that V_p/V_s anomalies at 5-10 km depth correspond to hot (~1000°C) rhyolite source regions, while basaltic magmas (~1150°C) were stored at 15 km depth under the caldera. These examples illustrate how our model can link petrology and geophysics to better constrain the architecture of volcanic feeding systems. Our model (MagMaTaB) is accessible through a user-friendly web application (https://igdrasil.shinyapps.io/MagMaTaBv23/)

KEYWORDS: Thermobarometry, Hygrometry, Machine Learning, Magmatic Plumbing System, Magma Source

INTRODUCTION

Advances in igneous petrology and volcanology depend critically on our ability to determine the pressures (P), temperatures (T), and water contents of magmas (Blundy and Cashman, 2008; Putirka, 2017). By understanding these parameters, petrologists can gain insights into a wide range of problems, including the construction and evolution of the crust and mantle (Tibaldi et al. 2013; Jagoutz, 2014; Plank and Forsyth, 2016; Till, 2017; Ducea et al. 2021), and the pre-eruptive storage and transport properties of magmas, which are essential to characterize the architecture of igneous plumbing systems (Edmonds et al. 2019; Maclennan, 2019; Nazzareni et al. 2020; Giordano and Caricchi, 2022). P-T-H_2O conditions are at the core of establishing meaningful links between petrological processes and geophysical monitoring of active volcanoes (Weber and Castro, 2017; Magee et al. 2018; Pritchard et al. 2018; Halldórsson et al. 2022; Dayton et al. 2023) and set fundamental controls on eruption dynamics (Ruprecht and Bachmann, 2010; Andújar and Scaillet, 2012; Cassidy et al. 2018; Popa et al. 2021). In addition, diffusion studies are heavily dependent on temperature information to reconstruct timescales of magmatic processes (Petrone et al. 2016; Weber et al. 2019; Costa et al. 2020; Chakraborty and Dohmen, 2022). A thorough understanding of magmatic variables is therefore essential for further progress in a variety of petrological fields.

P-T-H_2O conditions of magmas can be determined by a variety of methods that rely on equilibrium exchange reactions between different mineral phases or minerals and melts (e.g. Putirka, 2008; Blundy and Cashman, 2008). Although temperatures can be recovered with fairly small error margins (typically better than ±30-60°C; e.g. Holland and Blundy 1994; Ghiorso and Evans, 2008; Putirka, 2008; Neave and Putirka, 2017), pressure estimates struggle with uncertainties that lie at the very limit of usefulness. For example, the frequently used clinopyroxene-melt (eqn. 32a of Putirka, 2008) and amphibole-melt barometers (Putirka, 2016) show respective errors of at least 3 and 4 kbar, corresponding to a depth uncertainty of approximately 10 to 15 km, which is insufficient to resolve the structure of crustal magmatic systems. This may be attributed to analytical and experimental challenges (Wieser et al. 2023), reflect minor P-dependency of the components used in the regression (Putirka, 2016), or the choice of regression strategy (Higgins et al. 2022).

An alternative approach is to obtain magma storage conditions from the major element chemistry of the melt phase in equilibrium with a particular mineral assemblage. In principle, volcanic glass chemistry can provide P-T conditions through the shift of cotectic lines for quartz- and feldspar-saturated melts (Blundy and Cashman, 2001; Gualda and Ghiorso, 2014), or for mafic liquids saturated with olivine, plagioclase, and clinopyroxene (Yang et al. 1996; Hartley et al. 2013). In crystal-rich mushes, of the type that have been shown geophysically to underlie volcanic areas worldwide, melt chemistry is buffered by the volumetrically dominant mineral assemblage, suggesting the possibility to constrain extraction source conditions in terms of the pressure and temperature at which a melt is multiply-saturated at its liquidus (Blundy, 2022). This approach (Fig. 1) requires only that the melt originated in a multi-mineral mush at depth and remained closed, except for loss of volatiles, during subsequent ascent, crystallisation and pre-eruptive storage (Gualda et al. 2019; Blundy, 2022). Blundy (2022) used this method to develop a thermobarometer and hygrometer for volatile-saturated melts in

equilibrium with the common mineral assemblage clinopyroxene-hornblende-orthopyroxene-magnetite-plagioclase-ilmenite (CHOMPI) using published phase equilibrium experiments to calibrate the model. As magmas ascend from their source they may degas and cool, crystallising in the process. This modifies the composition of the melt phase to reflect the conditions under which crystallisation and degassing occurred (Fig. 1). These may, for example, equate to immediate pre-eruptive storage conditions or to an integrated polybaric ascent path. P-T-H2O information obtained from these melts, for example as melt inclusions or matrix glasses, should record shallower depths than the original source. Unless crystallisation during ascent leads to physical separation of crystals and melt, the bulk composition of the system, excepting volatiles, will remain unchanged and thus preserve information about the magma source depth.

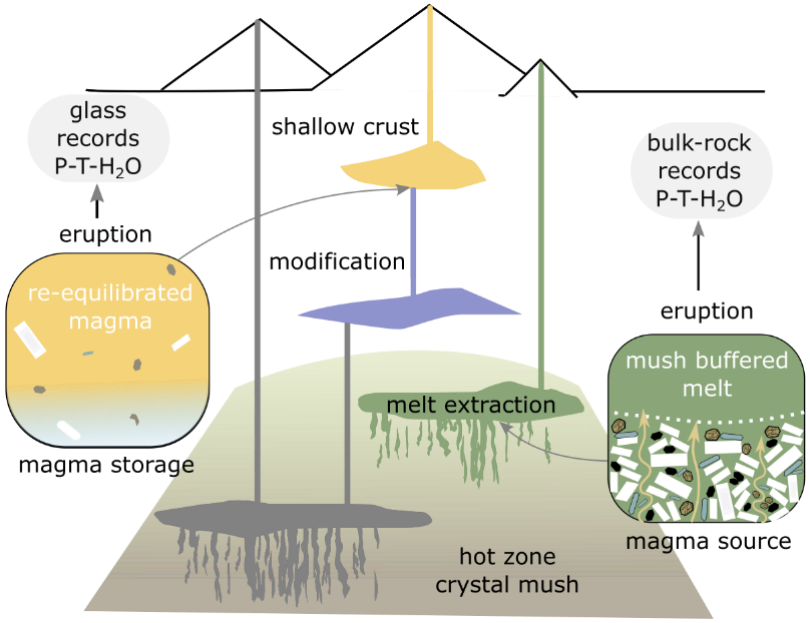

Fig. 1. Conceptual sketch illustrating different types of P-T-H_2O information stored in volcanic materials. Melts are extracted from crystal mushes (hot zones) are buffered by the volumetrically more dominant mineral assemblage, which will vary as a function of pressure, temperature, and water content. If such liquids are erupted without modification, for example through magma mixing or crystal accumulation, then the bulk-rock composition can be used to recover extraction source conditions. Storage conditions of magmas that have been modified and re-equilibrated can be reconstructed from the melt (glass) and mineral phase assemblage.

Although both source extraction and subsequent storage conditions can be successfully determined by melt thermobarometry, the calibration range of current models is relatively limited. The large number of available experiments and recent advances in machine learning make it now possible to test if P-T-H_2O recovery from melts can be generalised over a wider range of phase stabilities and melt compositions. Here we build a large compilation of phase equilibrium experiments and calibrate a machine learning model to predict P-T-H_2O of crustal magmas from the major element chemistry of melts. We assess model errors based on experimental data not used in the calibration and test different optimisation strategies to obtain the most accurate results. Finally, the model is applied to three case studies of volcanic systems that have well constrained geophysical tomography and independent thermobarometric estimates.

RATIONALE

The use of mineral-melt assemblages to constrain pressure and temperature, such as that espoused by Blundy (2022) or embedded in the amphibole solidus barometer of Mutch et al (2016), has its roots in the Gibbs Phase Rule, $\Phi + F = C + 2$, where Φ is the number of phases, C the number of components and F the number of degrees of freedom. To limit the latter to the two or three variables of interest, e.g. pressure, temperature and H_2O content, requires co-existence of a relatively large number of phases. If we consider magmas to be a ten-component mix of major oxide species, SiO_2-Al_2O_3-TiO_2-Fe_2O_3-FeO-MgO-CaO-Na_2O-K_2O-H_2O, then eight minerals need to coexist with melt and fluid to generate a sufficiently low degree of variance. If fO_2 is known, then Fe_2O_3/FeO ratio can be constrained, reducing the number of mineral phases to seven. Blundy (2022) settled on six mineral phases (CHOMPI, above), while the amphibole barometer requires seven; amphibole-biotite-plagioclase-alkali feldspar-quartz-magnetite-ilmenite (or titanite). Ensuring that so many minerals are in equilibrium with a given melt is an exacting requirement and, in the case of volcanic rocks that originated at depth in the presence of minerals that may no longer be stable as phenocrysts, difficult to prove.

However, application of the Gibbs Phase Rule to natural magmas overlooks the fact that not all ten oxide components are independent. In fact, natural terrestrial magmas inhabit only a very small volume of the compositional space due to the strong correlations between components in the relatively limited number of common igneous minerals. A glance at any Harker plot of igneous rocks makes this important feature readily apparent. Thus, natural magmas have a much smaller number of *effective* components than their complex compositions would suggest. We can demonstrate this fact by performing Principal Components Analysis (PCA) on a large body of igneous rocks. To calculate the number of independent components necessary to explain the total variation in 8-dimensional major element, anhydrous oxide space (SiO_2-Al_2O_3-TiO_2-FeO-MgO-CaO-Na_2O-K_2O), we carried out a PCA on a global compilation of arc magmas (Fig. 2). PCA reduces the dimensionality of datasets by linearly transforming the data into a new coordinate system, using Eigenvectors and the covariance matrix (e.g. Aitchison, 1984). As shown in Fig. 2a, the first principal component (PC) is most strongly impacted by the loadings (eigenvectors * $(\text{eigenvalues})^{1/2}$) of SiO_2, CaO, and FeO, explaining 69% of the data. PC2 is most significantly affected by Na_2O, describing 12% of the total variance. PC3 (9%) is mainly influenced by TiO_2 and Al_2O_3, while K_2O provides the strongest contribution to PC4 (6%) (Fig. 2b). A cumulative plot (Fig. 2c) shows that although 7 PCs are required to explain 100% of the data, just 4 PCs encompass 96% of the data. Considering 4 components and a typical phase assemblage (e.g. clinopyroxene-orthopyroxene-olivine-oxide-melt-fluid), the system would be invariant (F=0). We suggest that due to the covariation of major element oxides, which are not truly independent of each other, the variance of common magmatic phase assemblages tends to be generally low. This finding provides a rationale for our approach to calibrate thermobarometric and hygrometric models over a wide range using melt chemistry and mineral paragenesis.

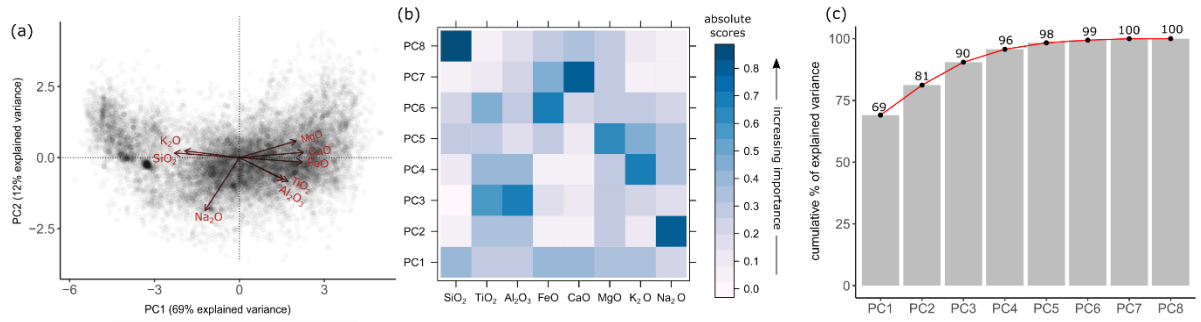

Fig. 2 Principal components analysis of arc magma bulk-rock and glass compositions. a) Cross plot of principal component (PC) 1 versus PC2 with loadings shown as red vectors. b) Matrix of loading scores for different major element oxides and PCs. Darker colours indicate an increasing importance of the particular oxide on the PCs. c) Cumulative percentage of variance explained by the different PCs. 96% of variance is explained by just four components.

MACHINE LEARNING AND ITS APPLICATION IN THERMOBAROMETRY

Machine learning is defined as the ability of a computer algorithm to learn from examples, existing in the form of data, and leverage this experience to build statistical models that make predictions on new observations (Zhou, 2021). It is widely used for pattern or cluster recognition in unlabelled data, as well as for classification and regression tasks on labelled datasets. Among the latter class of models, also called supervised learning, a wide range of algorithms have been developed, with particular strengths and weaknesses for different types of data and applications (Mohammed et al. 2016).

One of the most flexible and widely used supervised learning algorithms is random forests (Breiman, 2001). In principle, this method is based on aggregating re-sampled hierarchical flowcharts (decision trees) to minimise group heterogeneity (Fig. 3). As shown in Fig. 3a, decision trees consist of an initial root node, branches, internal nodes and leaf nodes. Starting from the root node, a tree is built by splitting the data into compartments (internal nodes) based on data features that correspond to the independent variables in the model. Leaf nodes then represent the final outcomes for different possible paths through the tree structure. In a random forest, a large number of decision trees is grown through bootstrapping (sampling with replacement) of the training (calibration) dataset and predictions are made by averaging the outcomes of all trees (Fig. 3b). This procedure leads to much improved accuracy of random forest models compared to single decision trees (Zhou, 2021). The learning process in random forest models can be tuned through a set of hyperparameters, such as the number of trees in the model or the number of variables that are randomly sampled as candidates for each split. In conventional random forests, split-point values for each variable, defining a tree node, can be calculated based on different mathematical criteria. A variation of this method, the extremely randomized trees (ERT) algorithm (Geurts et al. 2006), involves randomizing the choice of variables and split points that define each tree node, which is computationally more efficient and can improve accuracy in some cases.

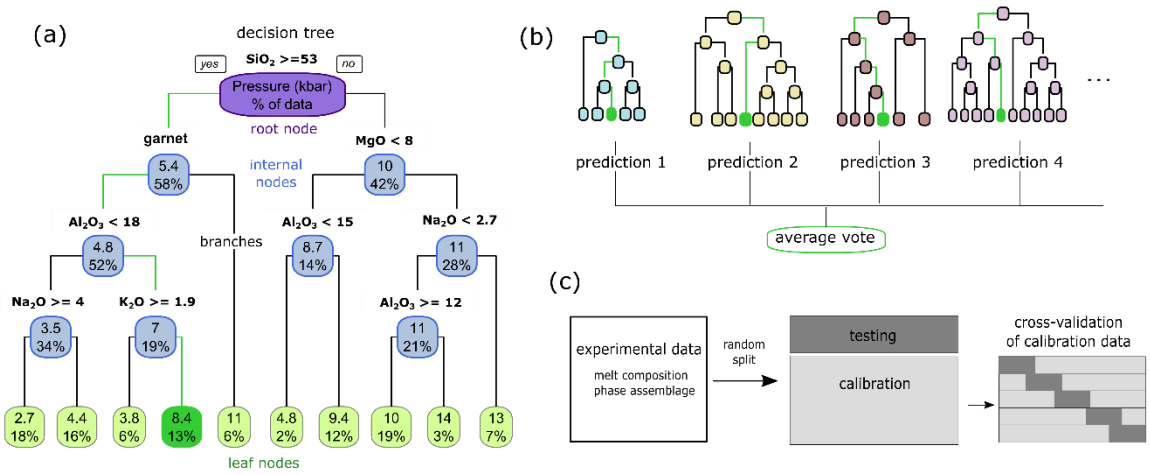

Fig. 3 Methodological summary of the machine learning method (ERT random forest) used for regression. a) Example structure of a decision tree using mineral assemblage and major element oxides to predict pressure. The decision tree is comprised of a root node (purple) that is split based on a series of yes and no questions regarding the regression variables into internal nodes (blue) and finally leaf nodes (green). Left and right branches correspond to yes and no respectively. Each node shows the predicted value (P kbar – top number), and the percentage of observations in the node (bottom number). The green branches illustrate a prediction path and the dark green leaf node the predicted pressure. b) The predictions of a large number of decision trees (typically ~500) are ensembled and averaged without weighting. c) Experimental data are repeatedly split at random into calibration and testing data. Calibration data are further tested by 5-fold cross-validation.

It is best practise to test the performance of machine learning and conventional regression models on a subset of the calibration data (typically 15-20%) that was not used in training of the model (Fig. 3c). Additionally, the training dataset can be cross-validated by splitting it in k-fold training data sets and compare the resulting errors to the ones obtained on the testing data. The accuracy of model predictions is typically assessed using the root-mean-square-error (RMSE), defined as:

$$RMSE = \sqrt{\sum_{i=1}^{n} \frac{(y_i - \hat{y}_i)^2}{n}}$$

where $\hat{y}$ is the predicted value, y is the observed value, and n is the number of observations. It is important to note that the RMSE is sensitive to the range of observation (e.g. 0-15 kbar versus 0-30 kbar), which must be considered when comparing the performance of different models. Conversely, classification models with categorical prediction variables are evaluated using a contingency table (or confusion matrix) that compares absolute numbers of predicted and true conditions (i.e. true positives (TP), false positives (FP), true negatives (TN), and false negatives (FN)). Commonly used performance measures for such models include the accuracy ((TP+TN) / (TP+TN+FN+FP)), precision (TP / (TP+FP)), sensitivity, i.e., true positive rate = TP / (TP+FN)), and specificity, i.e., true negative rate = TN / (TN+FP)).

Several random forest-type models have been calibrated recently to predict pressures and temperatures from mineral chemistry and mineral-melt pairs (Petrelli et al. 2020; Thomson et al. 2021; Higgins et al. 2022; Jorgenson et al. 2022; Li and Zhang, 2022). In the first of these

studies, Petrelli et al. (2020) calibrated cpx and cpx-melt thermobarometers using a wide range of different machine learning algorithms and obtained best performance metrics for an ERT algorithm. This model was subsequently optimised by Jorgenson et al. (2022), showing that removing outcomes with high variance in the aggregated trees can improve the accuracy of model predictions. A recent calibration of a random forest amphibole barometer (Higgins et al. 2022) showed that reliable magma storage depths can be obtained using the often-maligned hornblende barometer, suggesting that machine learning methods can uncover patterns in data that are not captured by conventional linear regression approaches in thermobarometry. The adaptability of machine learning methods in this context is further exemplified by the successful calibration of unconventional mineral thermobarometers such as biotite (Li and Zhang, 2022).

METHODOLOGY

Data compilation

To calibrate thermobarometric and hygrometric models based on melt chemistry and associated mineral assemblages, we compiled 2243 phase equilibrium experiments from 119 published studies. The library of experimental phase relations (LEPR; Hirschmann, 2008) was used as a starting point and augmented by an extensive literature search. The latter comprises >60% of the final database. Simple synthetic magma compositions, as well as non-terrestrial and alkaline magmas, were not considered in data mining and removed from the LEPR compilation. This choice was made to ensure that the compositions considered lie within the reduced component space of terrestrial magmas shown in Fig. 2. The SiO_2 contents of experimental melts was limited to between 45 and 80 wt.%. To ensure comparability of different melts, major element oxides (i.e. SiO_2, TiO_2, Al_2O_3, FeO_t, MgO, CaO, Na_2O, K_2O) were normalised to 100% anhydrous. We do not consider P_2O_5 and MnO in the normalisation and calibration of the model given that various experimental studies did not report one or both of these oxides, which would hamper the intercomparison of different melts. There is a high degree of variability in the literature when it comes to reporting stable mineral phase relations, especially with regard to accessory phases and the classification of Fe-Ti oxides. Therefore, we focus on 10 major mineral groups (ol, opx, cpx, plag, amph, bt, ksp, qtz, ox), whose stability is assigned to each experimental melt. In this scheme, oxide (ox) saturation is allocated to a melt if the experiment contained either magnetite, ilmenite or both phases. Experiments at 1 atmosphere pressure were not considered in the compilation, as they frequently show rapid disequilibrium crystal growth that may bias melt compositions (Mollo et al. 2010; Ziberna et al. 2017). Estimates of the dissolved water content in the experimental melts are available for only a subset of experiments (n=1300). To assess the impact of analytical uncertainty on model performance, we further compiled 440 experimental melts that provided errors for each analyte. The full experimental data compilation used in this study is available in the electronic supplementary materials.

Extremely Randomised Trees – Random Forest algorithm

Random forest models were setup in the open-source programming language R (R Core Team, 2013), using the 'ranger' package, which provides a fast and flexible implementation suited for high-dimensional data (Wright and Ziegler, 2017). To calibrate and test the models, the compilation of experimental melts was randomly split into training and testing data with proportions of 75:25. To ensure that variation in the prediction variables (P-T-H_2O) were present in equal proportions in the training and testing dataset, random sampling was conducted within stratified prediction variables. This was achieved by binning each prediction variable into quartiles, which were then re-sampled separately. Models were calibrated and tested using either normalised major element oxides (SiO_2, TiO_2, Al_2O_3, FeO_t, MgO, CaO, Na_2O, K_2O) of the melt composition ('melt-only') or melt+mineral assemblage as dependent variables. The stability of particular mineral phases (ol, opx, cpx, plag, amph, bt, ksp, qtz, ox) for each melt was encoded as 1 (stable) or 0 (unstable). After initial performance testing, in accordance with previous work (Petrelli et al. 2020; Li and Zhang, 2022), best results were consistently achieved using an extremely randomised trees approach to random forests (Geurts et al. 2006). We therefore use an implementation of this algorithm (ranger: splitrule='extraTrees') throughout this study. Sampling was carried out over the entire training or testing dataset without replacement, and nodes were split by choosing fully randomised split-points and variables (Geurts et al. 2006). The number of random splits to consider for each candidate splitting variable was set to 10. In each model, the number of trees was set to 500. Hyperparameter tuning did not significantly impact the results and was discarded, which is in-line with previous studies using geochemical data (Petrelli et al. 2020; Jorgenson et al. 2022). Cross-validation of the calibration dataset was carried out using 5 random splits and returned similar RMSE to the testing data. The impact of random splitting of training and testing datasets on RMSE was quantified by iterating the assignment 100 times. The R code used in this study is available in the supplementary materials. A user-friendly web application 'MagMaTaB' was developed using the R package 'shiny' (Chang et al. 2021) can be accessed at: https://igdrasil.shinyapps.io/MagMaTaBv23/

RESULTS

Compiled variable space

As summarised in Table 1, the compiled experimental melts (*n*=2243) span a wide geochemical spectrum from basalt to rhyolite. For the subsequent calibration and application of thermobarometric and hygrometric models, it is crucial to establish whether these melts are representative of natural magma compositions in different tectonic settings. To accomplish this, we examine their variation relative to bulk-rock and glass compositions that have been pre-compiled in the GEOROC database for arc magmas (*n*=24598), the East African Rift (*n*=8646), and Iceland (*n*=7656). As shown in Fig. 4, the variation of different major element oxides shows that our compilation is consistent with the global arc magma array. Inter quartile ranges (IQRs), as well as extreme values (i.e. upper and lower boxplot whiskers, Fig. 4) fully capture the variation. Rare arc magmas with exceptionally high MgO (>25 wt.%), K_2O (>7 wt.%), CaO (>18 wt.%), or low Al_2O_3 (<5 wt.%) were, however, not included in the compiled dataset. Icelandic magmas (*n*=7656) are generally well represented by our compilation but can have higher TiO_2 (IQR: 1.3 - 2.6 wt.%) and FeO contents (IQR: 10.1 - 14.4 wt.%), as well as lower Al_2O_3 (IQR: 13.3 – 14.8 wt.%), and are therefore under-represented by the experimental melts (IQR_{TiO2}: 0.4 - 1.0 wt.%; IQR_{FeO}: 2.6 – 8.8 wt.%; IQR_{Al2O3}: 14.9 - 18.0 wt.%). Considerable overlap exists with East African Rift magmas (*n*=8646), but the variation in several major element oxides such as Al_2O_3, CaO, Na_2O, and K_2O is greater in natural samples compared to the compiled dataset (Fig. 4). In summary, the compiled major element oxide space of experimental melts overlaps widely with natural rock compositions of different geotectonic association, showing greatest agreement with arc magmas. The dataset captures large parts of the compositional space for Rift settings and Iceland, but the compilation and therefore the subsequent model calibration should not be applied to compositions outside the range (Min-Max) presented in table 1.

Table 1: Summary statistics of the compiled experimental data.

Statistic	Temperature	Pressure	SiO_2	TiO_2	Al_2O_3	FeO	CaO	MgO	K_2O	Na_2O	H_2O*
	(°C)	*(kbar)*	*wt.%*	*wt.%*	*wt.%*	*wt.%*	*wt.%*	*wt.%*	*wt.%*	*wt.%*	*wt.%*
Min	675	0.2	44.6	0.0	8.2	0.3	0.1	0.0	0.0	0.2	0.0
10th Percentile	840	1.0	49.0	0.2	13.6	1.3	1.6	0.3	0.2	1.8	2.4
1st Quartile	900	2.0	51.3	0.3	14.9	2.5	2.9	0.6	0.4	2.5	3.5
Median	1008	4.0	59.5	0.6	16.6	6.0	6.8	3.0	1.4	3.3	5.2
Mean	1031	5.1	60.8	0.7	16.5	6.0	6.8	4.2	1.7	3.3	5.5
3rd Quartile	1150	8.0	70.7	1.0	18.0	8.7	10.2	6.6	2.7	4.3	6.9
90th Percentile	1270	10.0	74.5	1.3	19.3	10.4	11.9	10.1	3.9	4.8	9.1
Max	1425	14.5	79.9	4.4	24.1	20.9	17.5	19.5	6.9	7.0	15.0

Major element oxides normalised to 100% anhydrous without MnO and P_2O5
Total number of experiments in the compilation n=2243
*Number of experiments with reported H_2O in melt n=1300

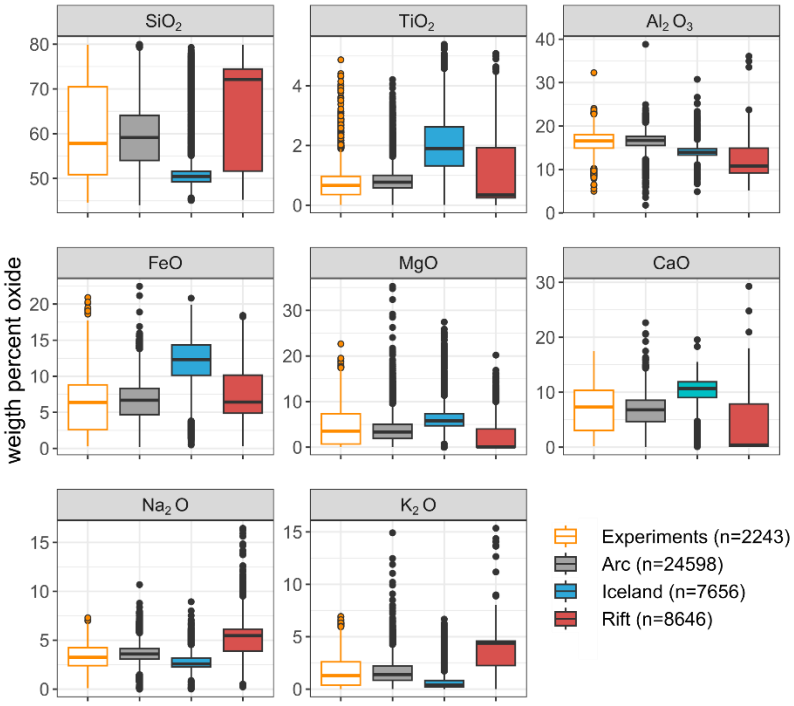

Figure 4: Boxplots of major element oxides for compiled experimental melts (n=2243; orange), compared to bulk-rock and glass compositions from subduction zones globally (Arcs; n=24598; grey), Iceland (n=7656; blue), and the East African Rift (n=8646; red). All natural rock compositions have been taken from pre-compiled files of the GEOROC database, were filtered between 45-80 wt.% SiO_2 and normalised to 100% anhydrous without MnO and P_2O_5. The Subduction Zones compilation include the: Aegean, Aleutian, Andean, Cascades, Honshu, Izu-Bonin, Kamchatka, Kurile, Lesser Antilles, Mariana, Mexican, New Zealand, and Sunda Arcs.

Focussing on the comparison with arc magmas, Harker diagrams using SiO_2 (wt.%) as an index of magma differentiation, show that the compiled experimental melts are fully consistent with geochemical trends of magma evolution (Fig. 5a-f). The experimental melts span a continuum of compositions, following the curvilinear variation of TiO_2, Al_2O_3 and MgO with SiO_2 (Fig. 5b-d), along with linear behaviour of CaO, FeO and alkali elements (Fig. 5a,e-f). Minor deviations from the predominant trends are observed for intermediate magmas (SiO_2 ~ 60 wt.%) with MgO >7 wt.% and andesites with Al_2O_3 < 13 wt.%, which are not captured by the experiments (Fig. 5c, d). Evolutionary trends in major element geochemistry for Icelandic magmas show overall equivalent behaviour (Fig. SM1). The most striking differences are higher TiO_2 (>3 wt.%) in mafic magmas, lower Al_2O_3 (<14 wt.%) in intermediate melts, and generally higher FeO contents, which are described by a fairly low number density of experimental melts. East African Rift magmas display a much wider variability in geochemical behaviour, such as alkaline differentiation trends, or non-linear SiO_2-CaO variation, that is only partially captured in the experimental dataset (Fig. SM2). As shown using colour-coding in Fig. 5, experimental magma evolution trends record a temperature control that, as expected, follows magma differentiation from basalt to rhyolite, but also tracks more subtle, stratified variation of temperature and mafic compositions such as low TiO_2 (<0.5 wt.%) and high MgO (>10 wt.%) for melt temperatures >1200°C.

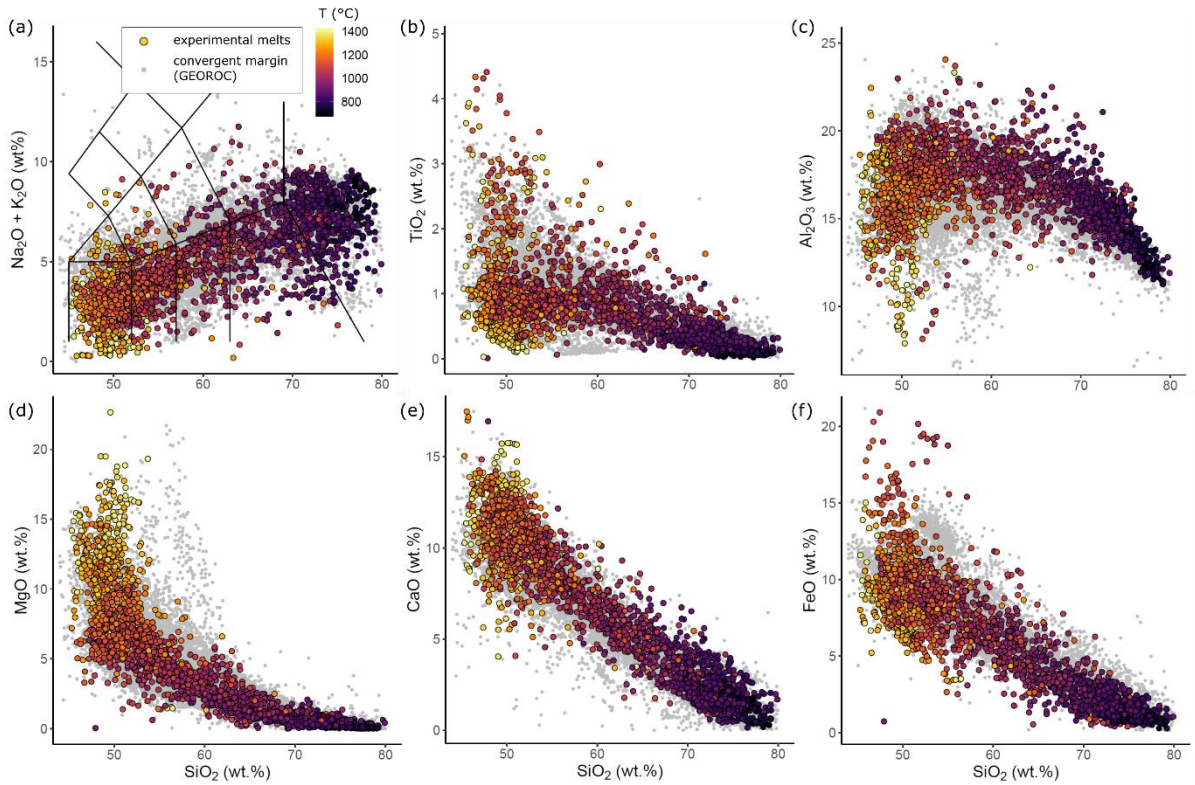

Fig. 5 Major element oxide (wt.%) versus SiO_2 (wt.%) in compiled experimental melts colour-coded for temperature (°C) compared to bulk-rock and glass compositions for global arc magmas (grey dots) from the GEOROC database. a) Total alkalis (K_2O+Na_2O) with compositional fields after Le Maitre et al. (2002). b) TiO_2, c) Al_2O_3, d) MgO, e) CaO, and f) FeO. All compositions were normalised to 100% anhydrous.

The compiled experimental melts cover a temperature range of 675-1425°C, pressures between 0.2-14.5 kbar, and dissolved H_2O contents of 0-15 wt.% (Fig. 6; Table 1). Temperature is distributed fairly symmetrically within this range, whereas pressure and H_2O contents are right (positively) skewed. Experimental pressures below 2.5 kbar, typically the range that can be reached in cold-seal pressure vessels, comprise 41% of the data. Considering bins of 2 kbar, the P range between 2.5 and 10 kbar is typically covered by >200-400 experiments. The range from 10-15 kbar is covered by 149 experiments. As shown in Fig. 6a, low T data are sparse for high-pressure (>10 kbar) experiments, while high-T melts (>1200°C) are distributed overall uniformly with pressure. Temperature conditions between 800 and 1200°C are well represented over the entire P-range. Dissolved water contents and T show a broad, negative correlation due to sparse data at low temperatures (<900°C) and low H_2O contents (<2.5 wt.%) (Fig. 6b). Likewise, high T melts (>1100°C) are high H_2O (>8 wt.%) are under-represented experimentally. H_2O contents are, of course, limited by solubility, which explains the upper bound in Fig. 6c; melts with lower H_2O are water-undersaturated. Besides these limitations, H_2O and T show a continuum of compositions that is well represented by the data. Phase relations in the compilation, considering only major minerals (ol, opx, cpx, plag, amph, bt, ksp, qtz, gt, ox), comprise a total number of 124 different assemblages. The most common mineral assemblages are broadly gabbroic: opx-cpx-plag-ox (n=182), ol-cpx-plag (n=147), ol-cpx-plag-ox (n=94), and plag-amph-ox (n=83). Figure 6 gives a good indication of the P-T-H_2O regions

that need to be explored experimentally to provide better calibration coverage. The full list of assemblages and their frequencies of occurrence is provided in Fig. SM3.

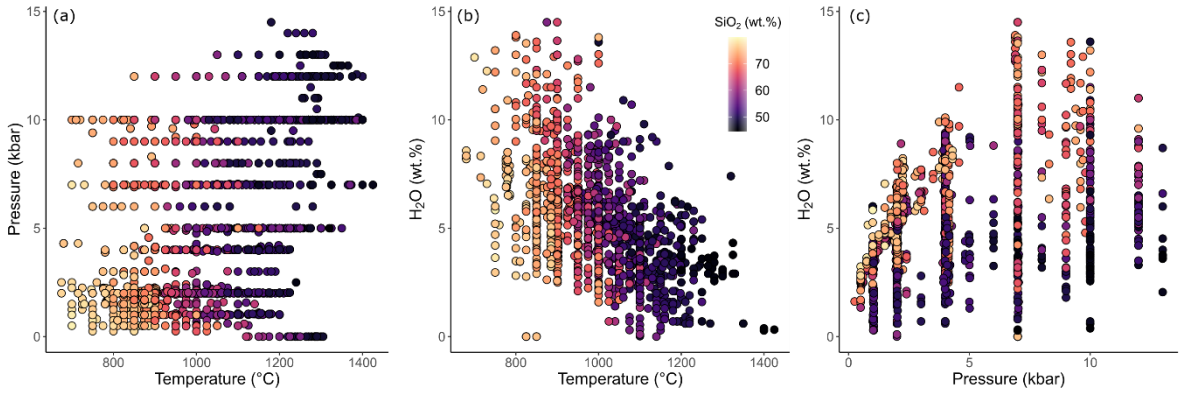

Fig. 6 P-T-H_2O parameter space in the complied experimental compilation. Colour coding reflects the SiO_2 (wt.%) of the melt. a) Experimental pressure (kbar) versus experimental temperature (°C). b) Melt H_2O (wt.%) versus temperature (°C), and c) H_2O (wt.%) versus pressure (kbar).

Model calibration and validation

Thermobarometric and hygrometric models, calibrated via the ERT algorithm, were run using either melt chemistry ('melt-only' model) or combinations of melt chemistry and mineral assemblage ('melt-assemblage' model) as independent variables. The latter model is appropriate in circumstances where both the melt composition and the saturating mineral assemblage are known, such as in a porphyritic volcanic rock containing melt inclusions; the former model applies when only the melt composition is available, such as an erupted whole-rock analysis. The melt-assemblage model recovers experimental pressures with RMSE of 0.6 kbar on calibration data and RMSE of 1.6 kbar on testing data not used in the calibration (Fig. 7a, b). Temperature is predicted with RMSE of 13 and 35°C on calibration and testing data, respectively (Fig. 7c, d), while uncertainties on water contents are 0.5 wt.% on calibration, and 1.3 wt.% H_2O on testing data. Error distributions, quantified as difference between the predicted and experimental variable (P-T-H_2O), show modal values and medians centred at zero in each case, indicating a high accuracy of the predictions (Fig. 7b, d, f). The error distributions are overall symmetrical for T but show a slight tendency towards overprediction at low values and underprediction at high-experimental values for P and H_2O. Using the algorithm to predict P-T-H_2O based on melt composition only generates equivalent results on the calibration dataset but consistently higher RMSE on testing data for each variable (Fig. 8). Pressures are recovered on testing data with RMSE of 1.9 kbar (Fig. 8a, b), temperatures with RMSE of 39°C (Fig. 8c, d), and H_2O contents with 1.6 wt.% (Fig. 8e, f). The shapes of error distributions are akin to those of the melt-assemblage model (Fig 8b, d, f). Although, the uncertainties of the melt-only model are systematically higher compared to the melt-assemblage model, they are only marginally worse, testifying to the predictive power of the liquid phase composition.

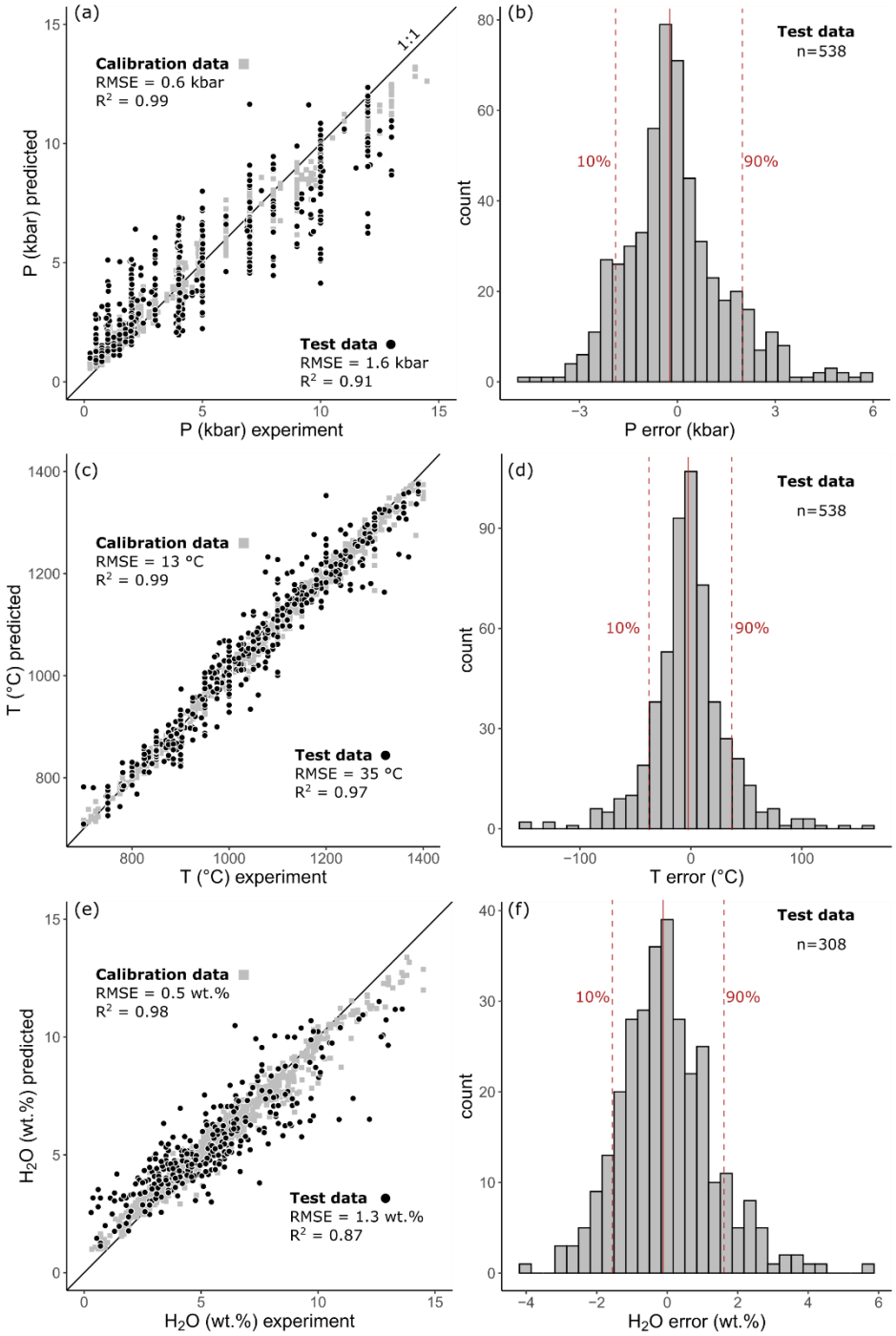

Fig. 7 Calibration and testing of the melt-assemblage model for recovery of P-T-H_2O. Calibration data are shown as grey dots and testing data as black points. RMSE and R^2 (Pearson's correlation coefficient) are shown for calibration and testing data. Black solid lines illustrate a 1:1 relation. a) Experimental pressure versus predicted pressure in kbar. b) Histogram of absolute difference (P-error) between experimental and predicted pressure on the testing data. Red dashed lines indicate the 10^{th} and 90^{th} percentile. c) Temperature of experimental melts versus predicted temperature (°C). d) Histogram of T-error for testing data. e) H_2O content of experimental melts versus predicted H_2O (wt.%). f) Histogram of H_2O error on testing data.

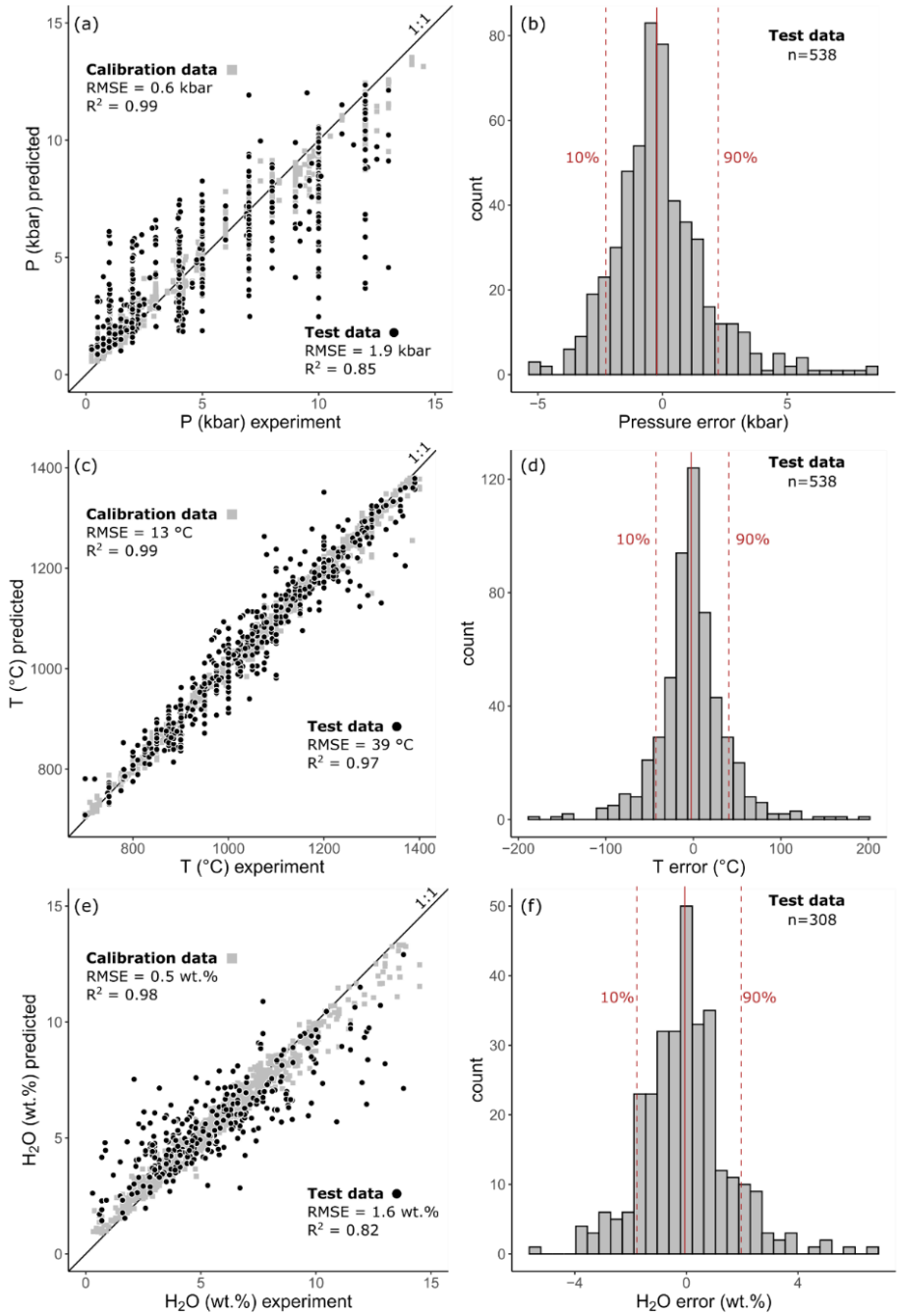

Fig. 8 Results of calibration and testing of the melt-only model for recovery of P-T-H_2O. The calibration data are shown as grey points and testing data as black points. RMSE and R^2 (Pearson's correlation coefficient) are shown for calibration and testing data. Black solid lines illustrate a 1:1 relation. a) Experimental pressure versus predicted pressure in kbar. b) Histogram of absolute difference (P-error) between experimental and predicted pressure on the testing data. Red dashed lines indicate the 10^{th} and 90^{th} percentile. c) Temperature of experimental melts versus predicted temperature (°C). d) Histogram of T-error for testing data. e) H_2O content of experimental melts versus predicted H_2O (wt.%). f) Histogram of H_2O error on testing data.

In addition to P-T-H_2O recovery, we set up models to constrain mineral phase saturation conditions based on melt chemistry, given that such information may be useful in model optimisation and for the general theoretical framework of liquid thermobarometry. For example, this method allows for an assessment of whether a given melt is multiply-saturated on its liquidus at the calculated source conditions. For this purpose, three sets of extremely randomized tree models were developed: 1) A classification algorithm that predicts the minimum number of saturated mineral phases from melt composition. 2) A model aiming to identify the particular saturated phase assemblage (e.g. plag-opx-amph-ox). 3) A regression model that predicts the number of saturated minerals from liquid chemistry. Based on melt composition, the algorithm can predict that a liquid is saturated with ≥3 minerals with average accuracy of 84%, precision of 85 %, sensitivity (true positive rate) of 93%, and specificity (true negative rate) of 66% (Fig. 9a). While the performance scores for ≥ 4 saturated minerals show acceptable accuracy (77%), precision (72%), and specificity (87%), the sensitivity is decreased to 59%. Overall, model 1 is most useful as a test if a specific liquid composition is saturated simultaneously with ≥3 minerals at its liquidus. A model to predict the particular phase assemblage in equilibrium with the melt (model 2) returned low accuracy scores and is therefore not considered further. Lastly, estimating the numerical number of mineral phases (model 3) results in a symmetrical error distribution and can be achieved with RMSE of 0.9 phases based on testing data not used for calibrating the model (Fig. 9b). In summary, the major element geochemistry of experimental melts records information on the number, but not the identity, of saturated mineral phases.

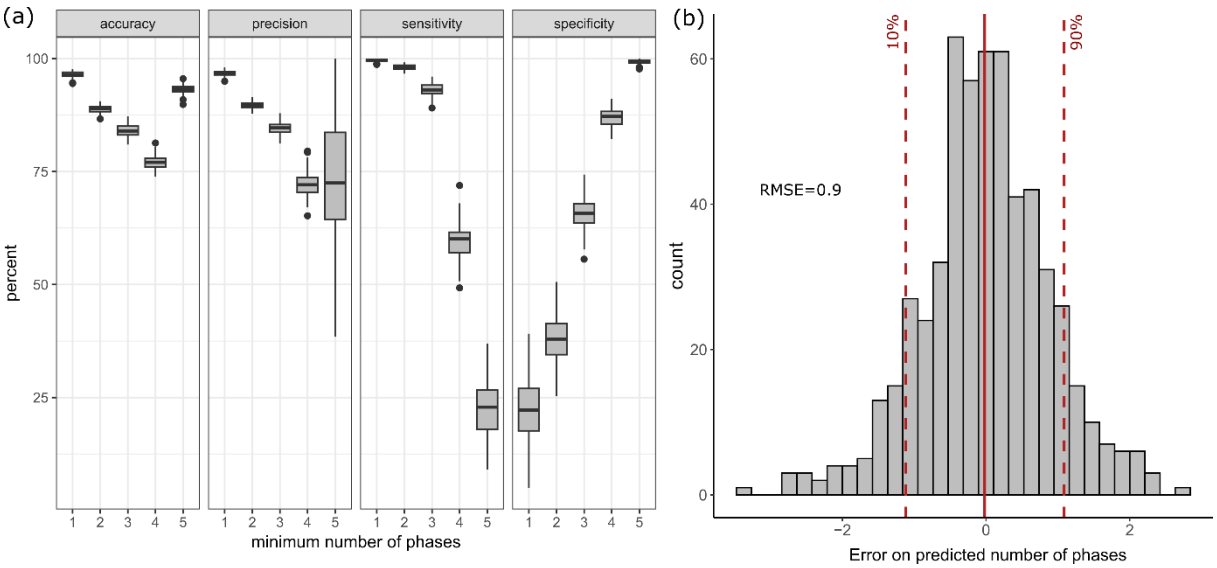

Fig. 9 Classification and regression models to predict mineral phase saturation conditions from experimental melt chemistry. a) Performance measures (accuracy, precision, sensitivity, and specificity) in percent for prediction of the minimum number of saturated mineral phases on testing data. See methods section for details on how the performance measures are calculated. b) Histogram of error on the predicted number of phases based on test data. Red dashed lines indicate the 10^{th} and 90^{th} percentile.

Optimisation of the modelling approach

From a thermodynamic standpoint, for a given number of chemical components, increasing the number of phases should reduce the degrees of freedom of the system. We therefore test if sub-setting the number of co-saturated minerals can optimise the performance scores of our model. First, however, it must be noted that the performance is also subject to the effects of processes involving random number generation. Specifically, this involves initial splitting of the full dataset into calibration and testing subsets, as well as building extremely randomised trees. We tested the impact of random number generation on model runs by iterating the splitting operation 100 times, obtaining distributions of RMSE for the testing data (Fig. 10a-c). The results show that random processes induce variability in the RMSE of P-T-H_2O. As expected, sub-setting the experimental dataset for different minimum numbers of stable mineral phases also impacts the performance of the model. The effect is strongest for T, showing a minimum median RMSE of 32°C for ≥3 minerals compared to a median RMSE of 38°C for the full dataset. Likewise, P-estimates show the lowest median RMSE of 1.55 kbar for saturation with ≥3 minerals (full dataset RMSE: 1.65 kbar). The effect is not evident for H_2O, showing only minor variation of RMSE with the minimum number of mineral phases (Fig. 10c). Sub-setting the database comes, however, at the cost of reducing the number of experiments, leading to overall worse performance in models with ≥4 saturated mineral phases. Sub-setting is therefore only recommended to a certain degree (i.e. not more than ≥3 mineral phases) to optimise the model in cases with petrographic or circumstantial (e.g. co-genetic plutonic xenoliths) evidence that such conditions prevailed. Further experimental data for multiply-saturated (>4 minerals) melts would help to remedy this situation.

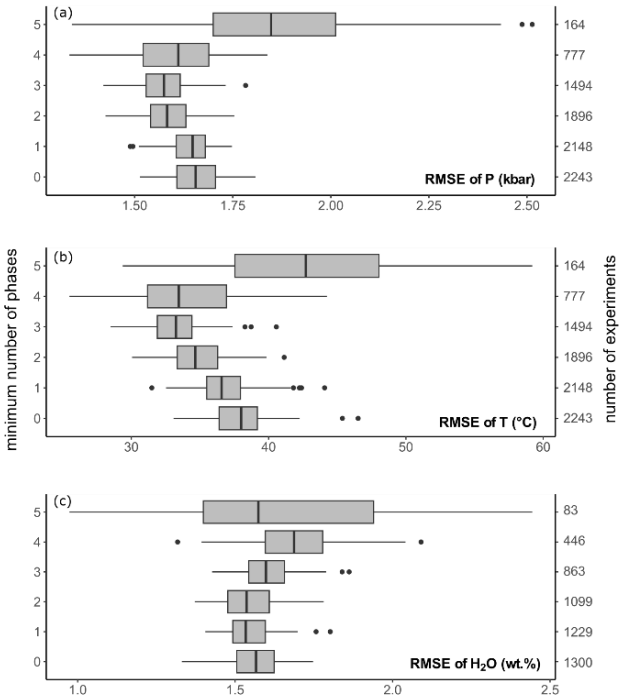

Fig. 10 Boxplots of RMSE calculated using 100 random splits of calibration and testing data. All model runs were carried out using the melt-assemblage algorithm. Experimental data were subset for different minimum number of saturated mineral phases. The number of experimental melts comprising the subset is shown on the right-hand side. a) RMSE of P (kbar), b) RMSE of T(°C), and c) RMSE of H_2O (wt.%).

Better performance of random forests may also be achieved through adjusting model-specific parameters (Jorgenson et al. 2022). We tested the impact of using the median instead of the conventionally used mean in averaging the distribution of individual P-T-H_2O votes of decision trees that comprise the random forest. The results are overall similar with a slight tendency of better performance for median voting (Table 2). Large improvements can, however, be achieved when a filtering approach based on the variance of the voting structure for individual P-T-H_2O estimates is applied. As shown in Fig. 11a-b, errors in P determinations increase systematically with the standard deviation (SD) of the voting distribution. We used the SD and IQR to quantify the voting variability and removed either 30% or 50% of the highest values for these measures (Table 2). Filtering based on SD and IQR returned overall similar results. Cutting the top 30% reduces RMSE of P determinations down to 1.2 kbar for both the melt-only and melt-assemblage model. Filtering out 50% of the highest variance tree ensembles can reduce the RMSE further to 0.9 kbar in case of the melt-assemblage model. Estimates of T can be obtained with RMSE of 21°C in the melt-assemblage model and down to 24°C in case of melt-only thermometry (50% filtering). A substantial improvement in the performance of the hygrometry models is suggested by a reduction of the RMSE to 1.0-1.1 wt.% in the case of 50% filtering. Importantly, filtering the estimates based on the variability of the voting distribution does not change the shape of the predicted variable distribution, showing that this approach does not systematically bias the results (Fig. 11c). In summary, more robust estimates of P-T-H_2O can be obtained by the optimisation approach based on filtering but are traded off against the removal of a number of good estimates. The filtering approach is best suited to large, co-genetic datasets from single volcanic eruptions or centres.

Table 2: Optimisation results of the melt-assemblage and melt-only models.

Filter	Test data	P (RMSE)		T (RMSE)		H_2O (RMSE)	
	n	mean	median	mean	median	mean	median
	%	*kbar*	*kbar*	*°C*	*°C*	*wt.%*	*wt.%*
melt-assemblage model							
non	100	1.6	1.6	35	34	1.5	1.5
SD	70	1.2	1.2	25	24	1.1	1.1
SD	50	1.0	1.0	22	22	1.0	1.0
IQR	70	1.2	1.2	25	24	1.2	1.2
IQR	50	0.9	0.9	21	21	1.0	1.0
melt-only model							
non	100	1.9	1.9	40	40	1.5	1.5
SD	70	1.4	1.3	28	27	1.3	1.2
SD	50	1.2	1.2	25	24	1.1	1.1
IQR	70	1.3	1.2	32	31	1.3	1.3
IQR	50	1.2	1.2	25	24	1.1	1.1

All model calculations were run with at least 1 mineral phase present

SD: Standard deviation

IQR: Interquartile range

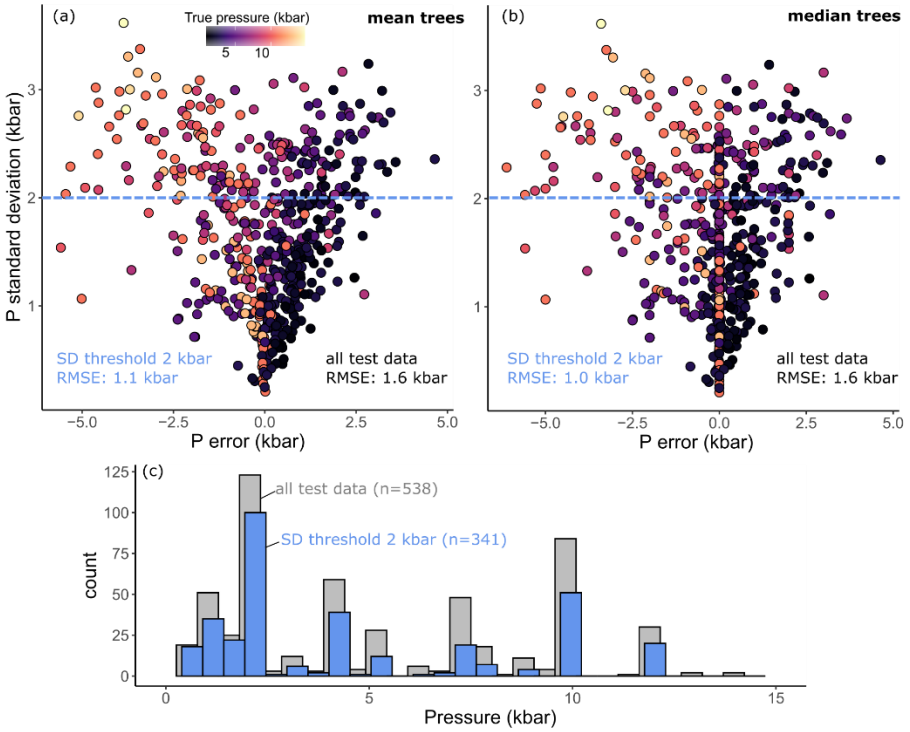

Fig. 11. Filtering approach to optimise model performance. a) P-error (kbar) is plotted against the standard deviation (SD) of individual tree ensembles that produce the average pressure vote for a particular melt composition. b) shows the same as in a) but using the median instead of the mean to average the ensembled trees. The blue dashed lines indicate a threshold value to filter out results with high SD. Colour coding reflects true experimental pressure in (kbar). c) Histograms of predicted pressure without filtering (grey) and filtered predictions based on the SD threshold (blue).

DISCUSSION

In this section, we discuss the performance and limitations of the model with respect to other thermobarometric calibrations, and the impacts of analytical uncertainties and the application of the melt-only model to bulk-rock compositions are critically evaluated. We then apply the model to three volcanic systems in different tectonic environments, which have been chosen based on the availability of geophysical tomography and independent petrological constraints that can be used to cross-validate the results. For each system, we discuss how the melt-only and melt-assemblage models can be applied to bulk-rock and glass compositions to map the source regions of extracted liquids, chart their subsequent ascent paths and provide estimates of pre-eruptive magma storage conditions.

Model performance and limitations

A few factors need to be considered, before comparing different thermobarometry models. The comparison should be based on a common measure of the model error that is ideally tested on data not used in the calibration. Given that widely used measures of prediction accuracy, such as the RMSE or the equivalent standard error of estimate (SEE), are impacted by the width of the calibration dataset (scale dependency), it is imperative to establish that models are compared

over a similar range in conditions (Hyndman and Koehler, 2006). For these reasons, other melt phase-assemblage thermobarometers such as ol-plag-cpx(augite)-melt (OPAM; Yang et al. 1996; Barton and Kelley, 2008; Hartley et al. 2018) and melt-cpx-amph(hornblende)-opx-magneite-plag-ilmenite (CHOMPI; Blundy, 2022) are difficult to compare to our model. Sub-setting our calibration dataset to either of these assemblages, we calculate test data RMSEs of 1.7 kbar, 28°C for OPAM and 1.9 kbar, 28°C for CHOMPI (mean of 100 splits into training and testing data).

As shown in Table 2, our full model, calibrated for P<15 kbar, returns P-T with RMSE of 1.9 kbar and 40°C (melt-only model), and RMSE of 1.6 kbar and 34°C (melt-assemblage). These errors can be reduced to 0.9 kbar and 21°C through SD or IQR filtering of the melt-assemblage model (Table 2). Calibrated over a similar range (P < 15 kbar, T~750-1300°C), the 'crustal' machine learning cpx thermobarometer of Jorgenson et al. (2022), shows uncertainties on testing data of 2.3 kbar for P and 63°C for T based on cpx compositions only, which can be improved by about 0.5 kbar and 30°C if the composition of the melt in equilibrium with cpx is considered. If a wider pressure range is considered in the calibration, this model determines P-T with 3.2 kbar and 48°C (<30 kbar; Jorgenson et al. (2022)). The machine learning cpx-liquid thermobarometer of Petrelli et al., (2020) recovers P with error of 2.6 kbar and T with 40°C (<40 kbar), similar to the widely used cpx-liquid regression of Putrika (2008) that constrain P with RMSE of 2.6 kbar (his eqn. 32b) and T with 42°C (his eqn. 33) over the same P-range. Restricting the P range to <12 kbar and the compositional range to mafic and intermediate magmas, the cpx-liquid barometer of Neave and Putirka (2017) and cpx-only model of Wang et al. (2021) yield errors of 1.4 kbar and 1.7 kbar respectively. Putirka (2016) compared and calibrated different amphibole thermobarometers, concluding that T can be recovered with typical precision of 30°C, and P (<30 kbar) with at best 4 kbar on test data. Subsequently, Higgins et al. (2022) showed that the large errors of amph-barometry can be reduced to 1.6 kbar using a machine learning approach, calibrated for P<12 kbar. The plagioclase-liquid hygrometer of Waters and Lange (2015), calibrated for relatively low pressures (P<3.5 kbar) and 0-8.3 wt.% H_2O, recovers water contents with 0.4-0.6 wt.% based on the average difference between measured and calculated H_2O on test data (c.f. our model: P< 15 kbar; 0-15 wt.% H_2O; RMSE: 1.0-1.5 wt.% H_2O). Compared to established and new state-of-the-art mineral-melt and mineral-only thermobarometers, our model represents an advance in prediction accuracy for P-T conditions of crustal magmas over a wide range of compositions. Importantly, our approach can be applied effectively and reliably to whole-rock or glass compositions without *a priori* assumptions about the equilibrium mineral assemblage. This makes the approach applicable to erupted whole-rock compositions as a probe of magma source depths, to melt inclusions trapped in a particular phenocryst phase or matrix glasses. Our method can also be applied to intrusive rocks provided there is textural evidence that these were once liquids and not cumulates. In summary, our approach has greater versatility than most conventional thermobarometers and hygrometers and can be applied to very large compositional datasets with relative ease.

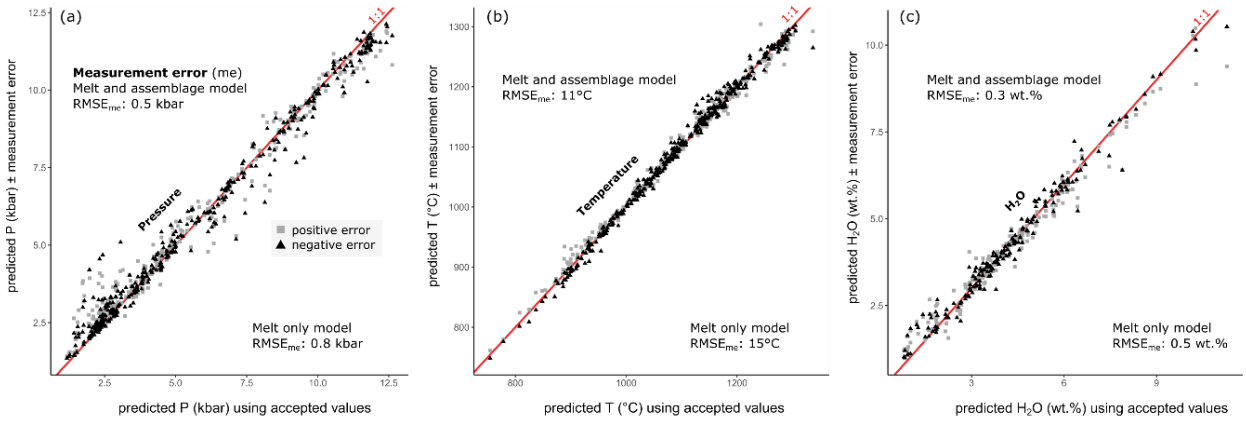

Fig. 12 Impact of analytical errors on results. Models were run using the accepted values and with added errors for each major element oxide. Positive errors are shown as grey squares and negative errors as black triangles. a) Predicted P (kbar) using accepted value versus predicted P (kbar) ± analytical error, b) Results for temperature (°C), and c) for H_2O (wt.%).

As shown in Fig. 11, the prediction accuracy of both melt-only and melt-assemblage models can be improved based on a IQR or SD filtering. However, the accuracy of the model predictions is ultimately limited by the analytical error on major element oxide measurements from the calibrant experiments (e.g. Wieser et al. 2023). We therefore tested the impact of analytical uncertainty on P-T-H_2O prediction, using a subset of experiments (n=440) for which error estimates were available for each analyte. Running the model using the accepted measured values, adding, and subtracting the error bounds, we quantify the deviation on predicted P-T-H_2O values resulting from analytical uncertainties alone (Fig. 12). These calculations suggest that measurement errors limit P-determinations to ±0.8 kbar, T-estimates to ±15°C, and ±0.5 wt.% H_2O. These are, in effect, estimates of the limit of precision that can be achieved using a melt composition approach calibrated using experimental petrology. Improvements of the model accuracy of P-T-H_2O determinations towards these limits should be possible in principle, for example by expanding strategically the experimental database. As illustrated in Fig. 6, the current experimental dataset overrepresents low-P conditions, most likely leading to the systematic over-prediction at low P and under-prediction at high P (Fig. 7a, 8a), which has been observed in other thermobarometric calibrations (e.g. Putirka, 2008; Neave and Putirka, 2017). Such effects are not seen for more uniformly distributed temperature (Fig. 7b, 8b). Although systematic errors resulting from non-uniform distributions in P are potentially resolved by re-sampling the experimental data to a regular grid (Higgins et al. 2022), reducing the number of experiments can lead to information loss. Clearly, further experimental work is needed to reinforce P determinations >3kbar, especially at low T<850°C, but also to expand the range of melt compositions to alkaline magmas (Figs. 5, 6) and provide precise measurements of melt H_2O contents.

A promising application for the use of melt-only models is that they can potentially be used to constrain P-T-H_2O of melt source regions from bulk-rock compositions (Fig. 1; Gualda et al. 2019; Blundy, 2022). This approach differs from constraints on equilibrium magma storage conditions based on melt-assemblage or mineral thermobarometers, in that it is based on

mineralogical buffering of a melt phase in a crystal-rich, mushy source region. Field, petrological and geophysical evidence suggests that most magmatic systems are comprised of high crystallinity mushes with distributed interstitial melt (e.g. Bachmann and Bergantz, 2004, 2008; Cashman et al. 2017; Lissenberg et al. 2019; Sparks et al. 2019; Edmonds et al. 2019). As discussed in more detail by Blundy (2022), the volumetric dominance of crystals over melt in mush systems may buffer the composition of the melt via reactive flow, and extraction of the liquid phase with subsequent rapid ascent and quenching upon eruption can retain a memory of P-T-H_2O of the mush source. However, this approach is under the premise that the bulk-rock composition is representative of the extracted liquid. Processes that could modify the original melt composition include magma mixing and crystal accumulation, as well as fractional crystallisation (i.e. open system removal of solid phases) of the melt at various crustal levels. To constrain the impact of modifications to the original melt composition on P-T-H_2O estimates using the melt-only model, we added 5, 10, and 15% of crystals (ol, plag, opx, cpx, amph, ksp, bt) to experimental liquids of different bulk composition (basalt, basaltic andesite, andesite, dacite, rhyolite) in an attempt to simulate the impact of entrained crystal cargoes on recovered P-T-H_2O. The results show that modification processes may lead to erroneous P-T predictions (Fig. SM4). It is therefore important to verify if a particular bulk composition represents a true liquid composition. We suggest that the following points are useful to consider in establishing this:

1) *Geochemical variation:* Major and trace element variation frequently show evolutionary trends such as curvilinear behaviour in Al_2O_3, MgO, Zr, Ba, or P_2O_5. Magma mixing and crystal accumulation processes can lead to linear trajectories, deviating from this behaviour, which can help to identify such processes (e.g. Sparks & Marshall, 1986; Deering and Bachmann, 2010; Lee and Bachmann, 2014; Masotta et al. 2016).
2) *Textural observations:* The method can be expected to work best for aphyric or crystal-poor magmas, given that these may represent extracted liquids that are unlikely to have experienced significant crystal accumulation.
3) *Mineral zoning:* Reverse zonation textures such as An-Fe-Mg rich plagioclase rims (Ruprecht and Wörner, 2007), Cr-rich rims in pyroxenes (Ubide and Kamber, 2018; Weber et al. 2019) or Mg-rich rims in olivine (Gordeychik et al. 2018) are all suggestive of magma mixing and re-equilibration processes. Bulk-rocks with crystal cargo dominated by this type of zoning are thus likely not representative of the original melt composition and should be avoided when using the melt-only model.
4) *Crystal-melt equilibrium:* The importance of open-system processes in the history of a bulk-rock may be interrogated by quantifying deviations from the mineral-melt equilibrium constant (Ganne et al. 2018). However, it should be borne in mind than an individual rock may have crystallised over a wide P-T-H_2O range and this will be reflected in a diversity of mineral compositions that were unable to equilibrate fully with the host melt prior to eruption.
5) *Thermometry:* Mineral thermometry, such as from co-existing oxide or pyroxene pairs, and melt-only (source) thermometry should provide corresponding results within uncertainty, if no cooling has accompanied the pre-eruptive storage since melt extraction from the mush (Blundy, 2022).

Lastly, in accordance with the phase rule discussed above, the most accurate results are obtained when the calibration dataset is confined to liquids that are saturated with ≥3 saturated mineral phases (Fig. 10). Although accurate results (RMSE: P<2 kbar) can also be obtained when only calibrating the model only on melts with ≤ 2 saturated minerals, we encourage the user to test saturation conditions using the classification and regression approaches shown in Fig. 9. Application of the melt-only model to bulk-rocks requires due diligence to establish that the composition represents a true liquid. Compared to most other state-of-the-art thermobarometry calibrations, our melt-only and melt-assemblage models show enhanced accuracy in P-T-predictions. Further targeted experimental work is likely to boost the performance of these models, given that the accuracy limit dictated by current analytical capabilities is not yet reached.

Applications: Tracking magma sources and storage conditions

The 1980-86 eruption of Mt. St. Helens volcano

The iconic 1980-86 eruption of Mount St. Helens, a stratovolcano in the Casces arc (USA) produced porphyritic dacites and silicic andesite (61-65 wt% SiO_2) containing phenocrysts of plagioclase-amphibole-orthopyroxene-magnetite-ilmenite with scarce clinopyroxene (Rutherford et al., 1985). The eruption initiated with a lateral blast on the morning of May 18th 1980, evolving to a large Plinian eruption column and culminating in a series of dome-forming episodes through October 1986. Eruption temperatures, from coexisting Fe-Ti oxides from the entire eruption lie in the range 881±54 °C and fO_2 0.2 to 0.8 log units above NNO (Melson, 1983; Rutherford et al., 1985; Blundy et al., 2008). A large number of phenocryst-hosted melt inclusions analysed by SIMS record dissolved H_2O contents up to 6.8 wt% and CO_2 up to 1200 ppm, corresponding to calculated saturation pressures of up to 3 kbar (Blundy & Cashman, 2005; Blundy et al., 2008, 2010; Cashman & Blundy, 2013). The overall range of melt inclusion volatile contents is consistent with volatile-saturated decompression crystallisation of dacite magma at near-constant temperature due to counterbalancing of adiabatic cooling by latent heat of crystallisation (Blundy et al., 2006). Plagioclase phenocryst zoning is consistent with crystallisation over this P-T range (Cashman & Blundy, 2013).

A large body of experimental data aimed at reproducing the phenocryst assemblage and matrix glass compositions in the Plinian phase of the eruption indicate magma storage pressures prior to eruption of 2.2 kb, with temperatures of 920 °C and an fO_2 just above NNO (Merzbacher & Eggler, 1984; Rutherford et al., 1985; Rutherford & Devine, 1988). Cogenetic plutonic xenoliths in 1980-86 eruptive products (Blundy 2022) are dominated by hornblende gabbronorites with interstitial glass testifying to the presence of such lithologies in the magma source region. Higher pressure experiments suggest that dacites from a previous (3.5 ka) eruption of Mount St. Helens, similar in composition to 1980-86, were multiply-saturated on their liquidus with the assemblage hornblende-plagioclase-orthopyroxene-magnetite-ilmenite at 7-9 kbar, 925 °C and 6-7 wt% dissolved H_2O. Blundy (2022) used these observations to justify use of his CHOMPI barometer to recover source conditions of 4.3 kbar, 950 °C and 5.5 wt% dissolved H_2O. Geochemistry is consistent with generation of dacite magma by mid- to

lower-crustal differentiation of arc basalt or basaltic andesite with minor crustal assimilation (Smith & Leeman, 1987; Wanke et al., 2019).

Mount St. Helens is exceptionally well monitored and studied geophysically. Precisely located earthquake hypocentres extend to almost 20 km below surface and appear to define a high-velocity plug at 6-9 km depth overlying an aseismic region thought to be occupied by magma (Lees, 1992). However, the relatively small magnitude of wave-speed anomalies throughout the sub-Mount St. Helens crust is more consistent with a mush region with pockets of higher and lower melt fraction than discrete melt-rich magma chambers (Lees, 1992; Kiser et al, 2016; Ulberg et al., 2020). Magnetotelluric images (Hill et al., 2015; Bedrosian et al., 2009) tell a similar tale of mushy source regions with a well-developed mid-crustal conductive anomaly at depths of ≥15 km connected to the volcanic edifice by elongate conductive tendrils that appear to circumnavigate resistive bodies interpreted as cold, solid precursor intrusions (Bedrosian et al., 2018). Long-period seismic events, consistent with fluid release, occur within the deep conductor at depths of 24-40 km below surface (Nichols et al., 2011).

Application of our melt-only thermobarometer and hygrometer to a compilation of whole-rock dome lavas and pumices (n=63) from the 1980-86 eruption yields pressures of 3.3-4.3 kbar, temperatures of 961-1016 °C (Fig. 13). P-calculations were carried out with SD filter of 0.75 and minimum number of saturated phases=3. No filtering was applied to T calculations, as the results were equivalent. The mean predicted number of co-saturated minerals is 3, consistent with multiple saturation. Application of the melt-assemblage model to melt inclusions and groundmass glasses from the studies cited above (n=71) yields pressures between 1.2-3.0 kbar, temperatures of 807-935°C, and water contents between 3.5-7.0 wt.%. All melt-assemblage calculations were carried out using opx-cpx-plag-amph-ox and no filtering was applied. The calculated pressures equate to depths of 12-16 km for whole-rocks, which we interpret as magma source depths and 5-11 km for melt inclusions, which we equate to decompression crystallisation during ascent, including brief periods of pre-eruptive storage. The temperature change from whole-rocks (961-1016 °C) to melt inclusions (807-935°C) is suggestive of some cooling during ascent and pre-eruptive storage. The depth results are consistent with the geophysical data presented above (Fig. 13a). However, our melt-assemblage model systematically over-estimates dissolved H_2O contents for less hydrous melt inclusions, where H_2O was directly determined by SIMS (Fig. 13b). It is unclear if this discrepancy represents a calibration issue or reflects the lack of equilibrium between the rapidly degassing melts, trapped mostly in plagioclase phenocrysts, and the wider phenocryst mineral assemblage with which the calculations assume the melt inclusions are in equilibrium. In this context, note that none of the calculated H_2O contents extend to the very low values recorded by the most degassed melt inclusions.

Overall, our results support a petrogenetic model for Mount St. Helens whereby dacite melts are generated within a laterally-extensive, mid-crustal reservoir of electrically-conductive mush and ascend to the surface via a narrow conduit region, crystallising and degassing en route with cooling of up to ~150 °C. This scenario is consistent with that proposed by Blundy (2022) for the Cascades arc more generally.

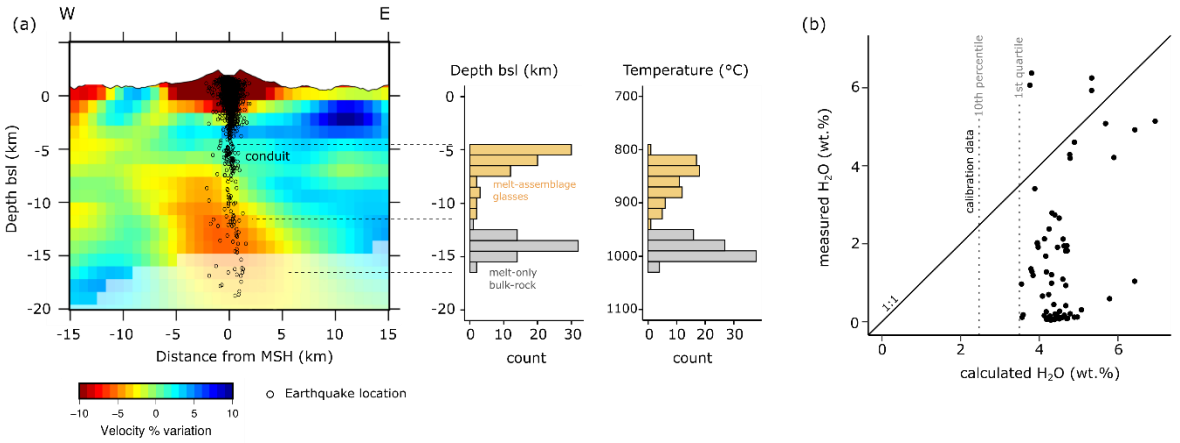

Fig. 13 Thermobarometry and hygrometry for Mount St Helens. a) Comparison of seismic velocity variation (%) and earthquake hypocentre locations with P-T estimates for Mt. St. Helens. The seismic cross-section was modified from Ulberg et al. (2020) and earthquake locations within a 5 km radius of the summit were taken from the Pacific Northwest Seismic Network database (https://pnsn.org/volcanoes/mount-st-helens). Histograms show depth estimates and temperatures for calculations involving bulk-rock compositions (grey) and glasses paired with plag-opx-cpx-amph-ox assemblages (yellow). Pressures were converted to depth by calculating a density profile from Vp velocities within 30 km of St Helens (Ulberg et al. 2020) using the equation of Brocher (2005). b) Calculated H_2O (wt.%) versus measured H_2O (wt.%) by SIMS (Blundy et al. 2008). The black line is a 1:1 relation. H_2O contents at the 10^{th} percentile and 1^{st} quartile of the calibration data are shown for comparison.

Andean ignimbrites and the Altiplano-Puna Magma Body

The Altilano-Puna Volcanic Complex (APVC), located in the Central Volcanic Zone of the Andes, has produced voluminous ignimbrite-forming eruptions during a flare-up episode over the last 10 Ma (Salisbury et al. 2011; Kern et al. 2016). Source calderas of the mostly dacitic and minor rhyolitic ignimbrites (Brandmeier and Wörner, 2016) match the spatial extent of the largest currently known crustal magma reservoir, the Altiplano-Puna Magma Body (APMB), which has been imaged by seismic, magnetotelluric, gravity, and geodetic methods (Pritchard et al. 2018 and references therein). However, while seismic tomography suggests that the roof of the APMB is on average at about 15 km depth beneath the surface of the Altiplano plateau (Ward et al. 2017), mineral-barometry and melt inclusion entrapment pressures indicate that the ignimbrites were sourced from more shallow crustal levels of ~5-8 km beneath surface (Lindsay et al. 2001; Schmitt et al. 2001; Muir et al., 2015; Grocke et al. 2017).

Here we focus on the eruptive products from the 60x35 km La Pacana caldera (Gardeweg and Ramírez, 1987; Lindsay et al. 2001) that gave rise to the 1600 km^3 (dense rock equivalent; DRE) Atana ignimbrite and the >180 km^3 (DRE) Toconao ignimbrite (Lindsay et al. 2001; Weber et al. 2023), as well as the Purico ignimbrite (~100 km^3 DRE), sourced from the neighbouring Purico shield complex (Schmitt et al. 2001). The bulk of the Atana and Purico ignimbrites are crystal-rich dacites (so-called ‘monotonous intermediates’) with minor crystal-poor rhyolite pumices and andesitic enclaves, whereas the bulk of the Toconao eruption

represents a crystal-poor rhyolite with minor andesitic enclaves (Lindsay et al. 2001; Schmitt et al. 2001). We applied the melt-assemblage model to groundmass glasses and quartz-hosted melt inclusions from the eruptions, using the mineral assemblages and data published in Lindsay et al. (2001) and Schmitt et al. (2001). Implicit here is that the melt inclusions, although trapped in quartz, were in equilibrium with the entire phenocryst assemblage at the time of trapping. The melt-only model was applied to the range of bulk-rock compositions. As discussed in a previous section, this approach requires some consideration of how representative these compositions are of true melts. Rhyolite pumices typically are crystal poor (16 - 1 vol.%; Lindsay et al. 2001) with no indication of hybridisation processes and could thus potentially represent true liquid compositions. However, this assumption only holds if (i) the crystal cargo grew from the bulk melt composition during ascent and does not include entrained crystals, and (ii) individual bulk-rock analyses did not include tiny enclaves, which can be abundant in the Toconao ignimbrite. We therefore compare the results of melt-only and melt-assemblage thermobarometry for the Toconao ignimbrite. Mineral chemistry and textural relations indicate that the crystal-rich dacites and andesites did not experience external input of mafic melt that would modify their original composition (Schmitt et al. 2001; Lindsay et al. 2001). The large volume of monotonous crystal-rich dacites and lack of evidence for hybridisation processes in the petrogenesis of these rocks suggests that the La Pacana magma reservoirs were built to a large extent by melts of similar composition. However, given that these systems were constructed over protracted periods of time (Kern et al. 2016), and by the amalgamation of isotopically heterogeneous components (Weber et al. 2023), we focus discussion on the rhyolitic rocks. All model calculations were performed by sub-setting the experimental calibration to liquids with ≥3 saturated mineral phases. This approach is justified by the consistent outcome of the phase saturation prediction indicating ≥3 saturated minerals for all bulk-rock compositions and given the greater number of texturally pristine phases observed in the eruptive products (Lindsay et al. 2001; Schmitt et al. 2001). Filtering was carried out to remove the top 30% of results with highest SD on decision tree ensembles.

Pressure estimates shown in Fig. 14 for melt-assemblage pairs from dacitic pumices of the Atana and Purico eruptions cluster between 1.7 and 2.4 kbar (mean: 2.1 kbar), corresponding to a depth range of 6 to 9 km (crustal density of 2750 kg m^{-3}), which is above the roof of the present-day APMB in its central part (14 km below surface; Ward et al. 2017). These pressures, as well as the temperatures of 726-789°C (mean: 7.69°C) are identical to independent thermobarometric estimates for these eruptions (Schmitt et al. 2001; Lindsay et al. 2001; Weber et al. 2023). Two melt-assemblage pairs from dacitic pumices with relatively elevated Al_2O_3 contents (13.4 and 14.2 wt.%) suggest greater pressures of 3.5 kbar (Purico) and 6.1 kbar (Atana), extending well into the APMB depth range. Similarly, rhyolitic glass-assemblage and crystal-free glass estimates for Toconao (P~3 kbar; T=760-765°C) and Purico (P=3.7-4.1 kbar; T=811-849°C) reveal a likely origin of these melts at APMB depths. A higher temperature of Purico rhyolites compared to dacites was also suggested by Schmitt et al. (2001). Melt-only calculations using the rhyolitic bulk-pumice composition for Atana agree with a magma source at 3 kbar. However, using bulk-rock Toconao rhyolites, in place of glasses, results in shallower pressures between 1 and 2 kbar, which may reflect that these compositions do not represent true liquids. If liquids similar to the Atana bulk dacite were present in the magmatic system, their source was most likely deep (~4.2 kbar) and fairly hot (~950°C). Andesitic bulk compositions

for Atana and Purico consistently indicate pressures between 2 and 3 kbar, equivalent to the roof region of the present-day APMB. As also observed for Mount St. Helens, predicted water contents for glasses of the Atana ignimbrite (4.9-5.8 wt.% H_2O) are somewhat higher compared to quartz-hosted melt inclusion analyses for this eruption (3.1-4.4 wt.% H_2O), while typical estimates of 4.5 wt.% H_2O for Purico agree with available data. High pressure Purico glasses (~3 kbar) indicate water contents of 5.8 to 7.4 wt.%. No melt inclusion H_2O contents are available for Toconao, but our calculations suggest 5.4 wt.% H_2O, similar to the Atana eruption.

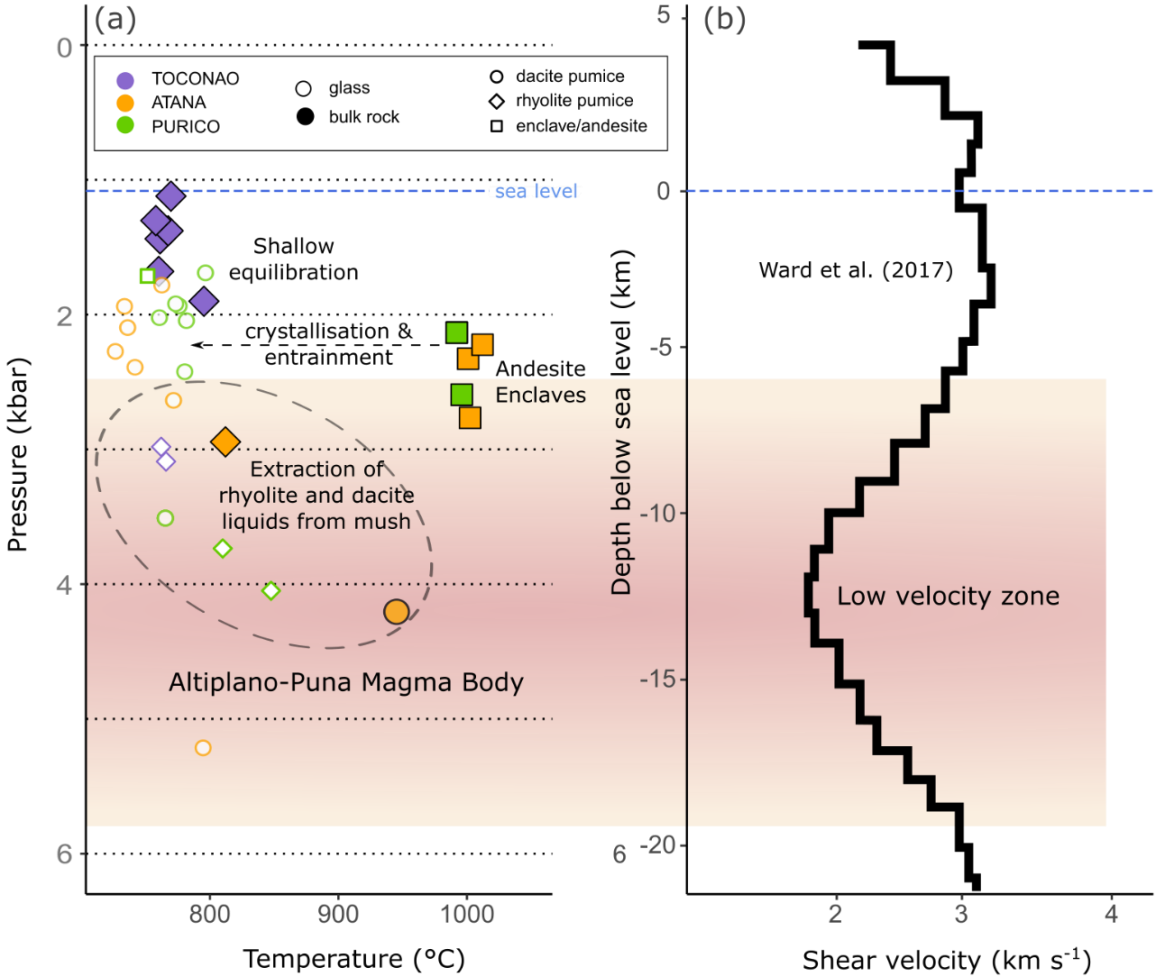

Fig. 14 Thermobarometry results for Central Andean ignimbrites. a) P-T estimates for glasses (open symbols) and bulk-rocks (filled symbols) from the Atana (orange) Toconao (purple) and Purico (green) ignimbrites. Dacite pumices are shown as points, rhyolites as diamonds, and andesitic enclaves as squares. Shaded region corresponds to the APMB. b) Shear wave velocity (km s^{-1}) in the Altiplano crust taken from Ward et al. (2017). Depth estimates were calculated from P-wave velocities by integrating the density profile for Altiplano crust (Gottsmann et al. 2017).

Our results corroborate that the Atana and Purico dacites were stored and erupted from about 2 kbar, equivalent to depth of 7 to 10 km beneath the surface, in-line with the observation that most silicic eruptions seem to be fed from this depth (Huber et al. 2019). This findings also supports the understanding that the APVC ignimbrites were not evacuated directly from reservoirs that correspond to the present-day APMB but at slightly shallower level. Yet, magma

crystallisation history as recorded by zircon spans at least 2.5 Ma for Toconao, and >1.5 Ma for both Atana and Purico (Kern et al. 2016). This is hard to reconcile with thermal modelling of shallow crustal magma accumulation, requiring extreme crustal growth rates and thermal energy input to maintain these systems above the solidus (Glazner, 2021). Although our thermometry shows that the ignimbrites have been erupted at low temperatures, other voluminous ash flows in the APVC, such as the Tara ignimbrite, have been erupted at ~850°C (Grocke et al. 2017). In contrast, our results suggest that rhyolite melts were sourced from deeper within the system, equivalent to the present-day APMB. This supports recent evidence from isotope geochemistry for several Andean super-eruptions that the shallow (~2 kbar) part of the feeding-system is comprised of near- or sub-solidus co-genetic earlier intruded material that is disrupted by incoming silicic melts in the short-term precursory episode ($<10^2$ yrs) to these events (Van Zalinge et al. 2022; Weber et al. 2023). The segregation and gravitational destabilisation of silicic melt lenses in deep crystal mushes, such as the APMB, has been shown to be physically plausible based on numerical and analogue modelling (Jackson et al. 2018; Seropian et al. 2018). This raises the question if the APVC magmatic system during the time of peak flare-up conditions would have shown a significantly different depth range in seismic imaging compared to what is observed today.

Historic eruptions from the Askja caldera (Iceland)

The Askja volcanic system in Iceland provides an ideal testcase to integrate petrological barometry with the results of geophysical tomography. Askja is located in the Icelandic rift zone and has frequently been active in the early 20th century, producing at least six small-volume basaltic eruptions in the vicinity of the central volcano (Hartley and Thordarson, 2013). Notably, in 1875 Askja produced a major explosive rhyolite eruption, one of Iceland's largest in the historical record, creating a 4.5 km wide collapse caldera that was subsequently filled by Lake Öskuvatn (Hartley and Thordarson, 2013). Seismic tomography, using local earthquake locations, has produced a snapshot of the crustal magmatic feeding system beneath Askja, revealing low-velocity structures at multiple levels beneath the caldera (Greenfield et al. 2016). The volcano is also actively deforming, showing deflation over timescales of years to decades and a strong surface uplift pattern centred at about 3 km depth based on Mogi modelling (de Zeeuw-van Dalfsen et al. 2011). It is currently not well constrained how these geophysical features of the volcanic plumbing system relate to the compositional diversity and storage depths of the bimodal magma associations erupted at Askja in its most recent history.

We used the melt-assemblage and melt-only thermobarometer on glass and bulk-rock compositions for 20th century Askja basalts and 1875 rhyolites utilizing data published in Kuritani et al. (2011), Hartley et al. (2013), and Schattel et al. (2014) (Supplementary tables). The basalts have phase assemblages of ol-cpx-plag-ox (Hartley et al. 2013) and 1875 rhyolites contain opx-cpx-plag-ox (Schattel et al. 2014). Both basalts and rhyolites are nearly aphyric, suggesting that application of the melt-only model is justified. Minor andesite glasses erupted in 1875 are not considered as these most likely represent mixed compositions, as suggested by SiO_2-Al_2O_3 divergence from the general evolutionary trend (Fig. SM1). Although not all Icelandic magmas are covered by our experimental compilation, Askja basalts and rhyolites are well captured (Fig. SM1). Temperature reconstructions for the basaltic melts using our model

yield averages of 1083-1120°C for the melt-assemblage model and 1111-1115°C for the melt-only model. No T-estimates are currently available for these eruptions, but the calculated temperatures are at the lower end of estimates for older lava flows from the Askja fissure swarm based on cpx-liquid thermometry (Hartley et al. 2013). Our T-H_2O estimates for the 1875 rhyolites (984-1006°C; 3 wt.% H_2O) corroborate previous thermometry and melt inclusion analysis (940-1008°C; max. 2.7 wt.% H_2O), showing that these melts were extremely hot and fairly dry. These results support the hypothesis that melting of hydrothermally altered crust, rather than protracted fractional crystallisation, play a key role in the origin of Askja rhyolites (Bindeman et al. 2012).

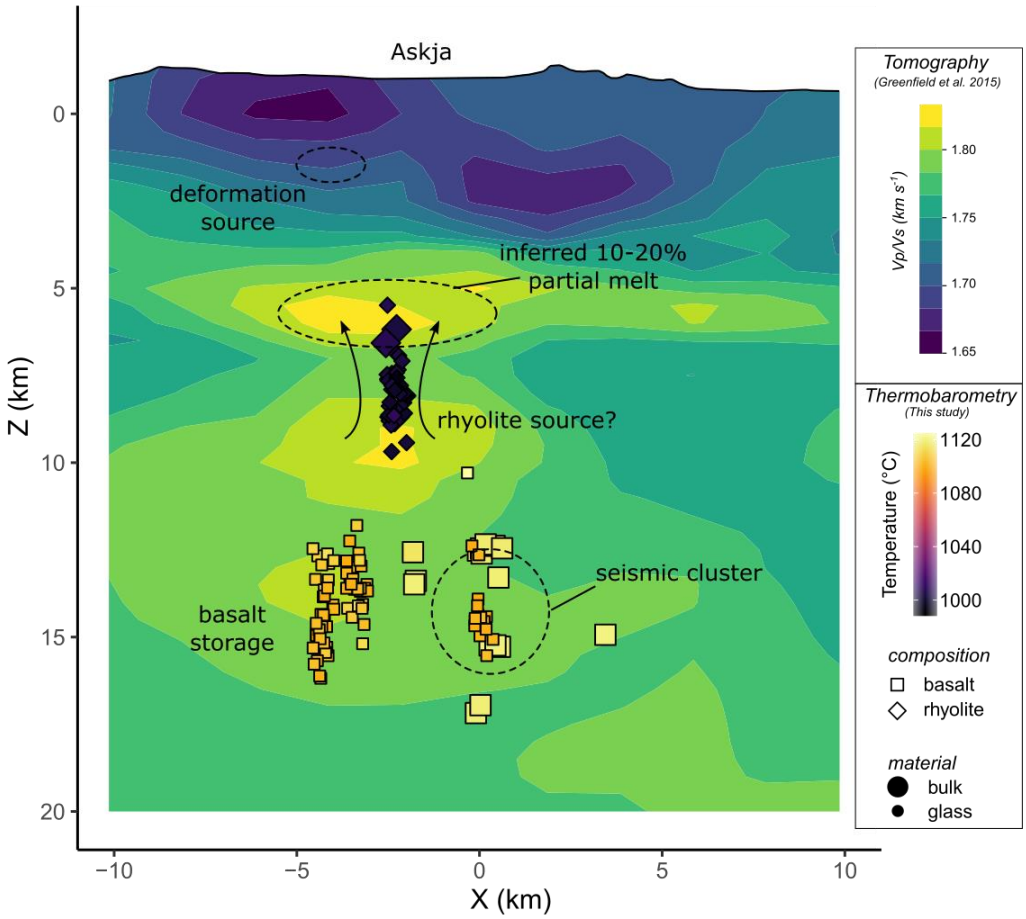

Fig. 15 Comparison of thermobarometric estimates and seismic tomography for the Askja caldera (Iceland). The seismic velocity structure of the crust beneath Askja parallel to the spreading direction was taken from Greenfield et al. (2015), with colours reflecting the ratio of P- and S-waves (V_p/V_s) in km s^{-1}. P-T estimates have been orthogonally projected onto the 2D crustal section and are shown as squares for basalts and diamonds for rhyolites. Smaller symbols represent calculations on glasses and larger symbols bulk-rocks, with colour coding reflecting the recovered T. Crustal density for Askja was calculated from seismic data of Greenfield et al. (2015) using the relation between wavespeeds and density of Brocher (2005).

Depth estimates using our model have been projected orthogonally onto the seismic tomography section of Greenfield et al. (2016), showing excellent correspondence with p-/s-wave velocity (Vp/Vs) anomalies (Fig. 15). Bulk-rock and glass-assemblage pairs of rhyolites

record indistinguishable depth estimates between 5 and 10 km below sea level (bsl). These depths correspond to a major zone of reduced wave speeds centred at 6 km and a smaller Vp/Vs anomaly located at 9 km bsl, the upper reaches of which have been inferred to contain about 10-20 % of partial melt on average. Basaltic bulk-rock and glass compositions return equivalent storage depths centred at 14±1.2 km depth (1 SD), corresponding to the lower part of the Vp/Vs anomaly and a region of active seismicity, which has been interpreted as a zone of melt movement (Greenfield et al. 2016). The storage depth range is narrower compared to previous cpx-liquid barometry on basaltic composition from historical Askja eruptions that indicated a very wide range between 2 and 18 km depth (Hartley et al. 2013). However, while cpx-liquid barometry may suffer from large errors (Wieser et al. 2023), the majority of these estimates (~11-14 km bsl) overlap with our constrained storage depth. Depth estimates within the range of shallow crustal deformation are absent in our calculations, which may reflect that no eruptions have been sourced from this depth in historical time. Nevertheless, the remarkable agreement between melt barometry and seismic tomography allows us to assign chemical compositions and temperatures to specific crustal magma bodies beneath the Askja caldera system.

CONCLUSIONS

The ability to quantify magmatic system variables from igneous rocks is invaluable to igneous petrology. However, thermobarometric models are often limited by large errors on pressure determinations and narrow calibration ranges. In this study, we have addressed this need by calibrating a widely applicable ERT random forest machine learning model to reconstruct magmatic pressures, temperatures, and water contents with increased predictive accuracy. The model utilizes glass chemistry and mineral paragenesis or bulk-rock compositions as dependent variables, both of which are readily available for most volcanic systems. We conclude that:

1) The major element oxide chemistry of melts (±mineral phase assemblage) is a powerful recorder of P-T-H_2O for crustal magmas over a wide range of multiple mineral saturation conditions and throughout the compositional spectrum from basalt to rhyolite. This empirical finding can be attributed to a more flexible regression strategy of large experimental datasets but may be theoretically grounded in the limited degrees of freedom of correlated oxide components in natural magmas.
2) Thorough error assessment of the model, using 100 random splits of training and testing datasets, indicate that P can be recovered with RMSE of 1.6 kbar (melt-assemblage model) and 1.9 kbar (melt-only model) from testing data not used in the calibration. Comparison of model predictions with independent estimates shows excellent agreement for hot-rhyolites (~1000°C) and cold-dacites (~750°C), both of which are scarcely included in the experimental calibration.
3) Prediction errors can be significantly reduced by filtering out P-T-H_2O estimates with high variance in the predictions of decision trees that comprise the random forest (RMSE of 0.9 kbar for pressure; Table 2). Better results are also obtained when the calibration data are restricted to a minimum of ≥ 3 saturated mineral phases, but the effect is small compared to filtering. The model could be further improved through additional experiments in areas that are currently underrepresented in P-T-H_2O space.

4) Calculations using pairs of glass chemistry and mineral assemblage can be used to reconstruct the last equilibration conditions of crustal magmas. The model also provides the opportunity to constrain mush extraction conditions (magma sources) under the premise that bulk-rock or glass compositions are representative of the extracted melt. The latter should be tested based on a set of petrographic and geochemical criteria.
5) Our ERT random forest algorithm allows to better integrate petrology and geophysical imaging of magmatic feeding systems. Application of the model to Mount St. Helens volcano indicates dacite sourcing rom a mid-crustal mush followed by decompression crystallisation and degassing accompanied by cooling. Application to APVC ignimbrites reveals a deep source of rhyolite melts in the APMB, clarifying the role of the world's largest magma body and regional super-eruptions. Barometric calculations for historical eruptions from the Askja volcanic system in Iceland allow assignment of rhyolite and basaltic compositions to specific seismic velocity anomalies beneath the volcano.

ACKNOWLEDGEMENTS

We would like to thank Ollie Higgins for sharing his insights on random forest thermobarometry, especially for valuable suggestions on how to optimise such models. Luca Caricchi is thanked for stimulating discussions on machine learning and accuracy. We thank Lena Melekhova for kindly sharing her experimental compilation. Carl Ulberg is thanked for his prompt and generous responses to e-mail requests for data and for sharing an editable version of his MSH seismic section.

AUTHOR CONTRIBUTIONS

Gregor Weber: Conceptualization, Investigation, Visualization, Formal analysis, Methodology, Software, Writing- Original draft. **Jon Blundy**: Conceptualization, Investigation, Funding acquisition, Writing- Review & Editing.

DATA AND CODE AVAILABILITY

All data and the R code used in this study are available in the supplementary materials to this article. The code can also be accessed as user-friendly web application at: https://igdrasil.shinyapps.io/MagMaTaBv23/

FUNDING

JB acknowledges support from a Royal Society Research Professorship (RP\R1\201048). GW acknowledges support from a SNSF early postdoc mobility fellowship (P2GEP2 195238).

REFERENCES

Ague, J. J. (1997). Thermodynamic calculation of emplacement pressures for batholithic rocks, California: Implications for the aluminum-in-hornblende barometer. *Geology*, *25*(6), 563-566.

Aitchison, J. (1984). Reducing the dimensionality of compositional data sets. *Journal of the International Association for Mathematical Geology*, *16*, 617-635.

Andújar, J., & Scaillet, B. (2012). Relationships between pre-eruptive conditions and eruptive styles of phonolite–trachyte magmas. *Lithos*, *152*, 122-131.

Atkins, P., & De Paula, J. (2013). *Elements of physical chemistry*. Oxford University Press, USA.

Bachmann, O., & Bergantz, G. W. (2004). On the origin of crystal-poor rhyolites: extracted from batholithic crystal mushes. *Journal of Petrology*, *45*(8), 1565-1582.

Bachmann, O., & Bergantz, G. W. (2008). Rhyolites and their source mushes across tectonic settings. *Journal of Petrology*, *49*(12), 2277-2285.

Bedrosian, P. A., Peacock, J. R., Bowles-Martinez, E., Schultz, A., & Hill, G. J. (2018). Crustal inheritance and a top-down control on arc magmatism at Mount St Helens. *Nature Geoscience*, *11*(11), 865-870.

Bindeman, I., Gurenko, A., Carley, T., Miller, C., Martin, E., & Sigmarsson, O. (2012). Silicic magma petrogenesis in Iceland by remelting of hydrothermally altered crust based on oxygen isotope diversity and disequilibria between zircon and magma with implications for MORB. *Terra Nova*, *24*(3), 227-232.

Blundy, J., & Cashman, K. (2001). Ascent-driven crystallisation of dacite magmas at Mount St Helens, 1980–1986. *Contributions to Mineralogy and Petrology*, *140*, 631-650.

Blundy, J., Cashman, K. V., Berlo, K., Sherrod, D. R., Scott, W. E., & Stauffer, P. H. (2008). Evolving magma storage conditions beneath Mount St. Helens inferred from chemical variations in melt inclusions from the 1980–1986 and current (2004–2006) eruptions. *US Geological Survey professional paper*, *1750*, 755-790.

Blundy, J., & Cashman, K. (2008). Petrologic reconstruction of magmatic system variables and processes. *Reviews in Mineralogy and Geochemistry*, *69*(1), 179-239.

Blundy, J., & Cashman, K. (2005). Rapid decompression-driven crystallization recorded by melt inclusions from Mount St. Helens volcano. *Geology*, *33*(10), 793-796.

Blundy, J. (2022). Chemical Differentiation by Mineralogical Buffering in Crustal Hot Zones. *Journal of Petrology*, *63*(7), egac054.

Brandmeier, M., & Wörner, G. (2016). Compositional variations of ignimbrite magmas in the Central Andes over the past 26 Ma—A multivariate statistical perspective. *Lithos*, *262*, 713-728.

Breiman, L. (2001). Random forests. *Machine learning*, *45*, 5-32.

Brocher, T. M. (2005). Empirical relations between elastic wavespeeds and density in the Earth's crust. *Bulletin of the seismological Society of America*, *95*(6), 2081-2092.

Cashman, K., & Blundy, J. (2013). Petrological cannibalism: the chemical and textural consequences of incremental magma body growth. *Contributions to Mineralogy and Petrology*, *166*, 703-729.

Cassidy, M., Manga, M., Cashman, K., & Bachmann, O. (2018). Controls on explosive-effusive volcanic eruption styles. *Nature communications*, *9*(1), 2839.

Chang, W., Cheng, J., Allaire, J. J., Xie, Y., & McPherson, J. (2021). shiny: Web application framework for R [Computer software]. *URL https://CRAN. R-project. org/package= shiny (R package version 1.6. 0)*.

Costa, F., Shea, T., & Ubide, T. (2020). Diffusion chronometry and the timescales of magmatic processes. *Nature Reviews Earth & Environment*, *1*(4), 201-214.

Dayton, K., Gazel, E., Wieser, P., Troll, V. R., Carracedo, J. C., La Madrid, H., ... & Perez-Torrado, F. J. (2023). Deep magma storage during the 2021 La Palma eruption. *Science advances*, *9*(6), eade7641.

de Zeeuw-van Dalfsen, E., Pedersen, R., Hooper, A., & Sigmundsson, F. (2012). Subsidence of Askja caldera 2000–2009: Modelling of deformation processes at an extensional plate boundary, constrained by time series InSAR analysis. *Journal of Volcanology and Geothermal Research*, *213*, 72-82.

Deering, C. D., & Bachmann, O. (2010). Trace element indicators of crystal accumulation in silicic igneous rocks. *Earth and Planetary Science Letters*, *297*(1-2), 324-331.

Edmonds, M., Cashman, K. V., Holness, M., & Jackson, M. (2019). Architecture and dynamics of magma reservoirs. *Philosophical Transactions of the Royal Society A*, *377*(2139), 20180298.

Ganne, J., Bachmann, O., & Feng, X. (2018). Deep into magma plumbing systems: Interrogating the crystal cargo of volcanic deposits. *Geology*, *46*(5), 415-418.

Giordano, G., & Caricchi, L. (2022). Determining the state of activity of transcrustal magmatic systems and their volcanoes. *Annual Review of Earth and Planetary Sciences*, *50*, 231-259.

Glazner, A. F. (2021). Thermal constraints on the longevity, depth, and vertical extent of magmatic systems. *Geochemistry, Geophysics, Geosystems*, *22*(4), e2020GC009459.

Gordeychik, B., Churikova, T., Kronz, A., Sundermeyer, C., Simakin, A., & Wörner, G. (2018). Growth of, and diffusion in, olivine in ultra-fast ascending basalt magmas from Shiveluch volcano. *Scientific Reports*, *8*(1), 11775.

Greenfield, T., White, R. S., & Roecker, S. (2016). The magmatic plumbing system of the Askja central volcano, Iceland, as imaged by seismic tomography. *Journal of Geophysical Research: Solid Earth*, *121*(10), 7211-7229.

Ghiorso, M. S., & Evans, B. W. (2008). Thermodynamics of rhombohedral oxide solid solutions and a revision of the Fe-Ti two-oxide geothermometer and oxygen-barometer. *American Journal of science*, *308*(9), 957-1039.

Grocke, S. B., de Silva, S. L., Iriarte, R., Lindsay, J. M., & Cottrell, E. (2017). Catastrophic caldera-forming (CCF) monotonous silicic magma reservoirs: Geochemical and petrological constraints on heterogeneity, magma dynamics, and eruption dynamics of the 3· 49 Ma Tara Supereruption, Guacha II Caldera, SW Bolivia. *Journal of Petrology*, *58*(2), 227-260.

Gualda, G. A., & Ghiorso, M. S. (2014). Phase-equilibrium geobarometers for silicic rocks based on rhyolite-MELTS. Part 1: Principles, procedures, and evaluation of the method. *Contributions to Mineralogy and Petrology*, *168*, 1-17.

Gualda, G. A., Gravley, D. M., Deering, C. D., & Ghiorso, M. S. (2019). Magma extraction pressures and the architecture of volcanic plumbing systems. *Earth and Planetary Science Letters*, *522*, 118-124.

Halldórsson, S. A., Marshall, E. W., Caracciolo, A., Matthews, S., Bali, E., Rasmussen, M. B., ... & Stefánsson, A. (2022). Rapid shifting of a deep magmatic source at Fagradalsfjall volcano, Iceland. *Nature*, *609*(7927), 529-534.

Hartley, M. E., Bali, E., Maclennan, J., Neave, D. A., & Halldórsson, S. A. (2018). Melt inclusion constraints on petrogenesis of the 2014–2015 Holuhraun eruption, Iceland. *Contributions to Mineralogy and Petrology*, *173*, 1-23.

Hartley, M. E., & Thordarson, T. (2013). The 1874–1876 volcano-tectonic episode at Askja, North Iceland: Lateral flow revisited. *Geochemistry, Geophysics, Geosystems*, *14*(7), 2286-2309.

Hartley, M. E., Thordarson, T., & Fitton, J. G. (2013). Oxygen isotopes in melt inclusions and glasses from the Askja volcanic system, North Iceland. *Geochimica et Cosmochimica Acta*, *123*, 55-73.

Helz, R. T., & Thornber, C. R. (1987). Geothermometry of Kilauea Iki lava lake, Hawaii. *Bulletin of volcanology*, *49*, 651-668.

Higgins, O., Sheldrake, T., & Caricchi, L. (2022). Machine learning thermobarometry and chemometry using amphibole and clinopyroxene: a window into the roots of an arc volcano (Mount Liamuiga, Saint Kitts). *Contributions to Mineralogy and Petrology*, *177*(1), 10.

Hill, G. J., Bibby, H. M., Ogawa, Y., Wallin, E. L., Bennie, S. L., Caldwell, T. G., ... & Heise, W. (2015). Structure of the Tongariro Volcanic system: Insights from magnetotelluric imaging. *Earth and Planetary Science Letters*, *432*, 115-125.

Holland, T., & Blundy, J. (1994). Non-ideal interactions in calcic amphiboles and their bearing on amphibole-plagioclase thermometry. *Contributions to mineralogy and petrology*, *116*, 433-447.

Huber, C., Townsend, M., Degruyter, W., & Bachmann, O. (2019). Optimal depth of subvolcanic magma chamber growth controlled by volatiles and crust rheology. *Nature Geoscience*, *12*(9), 762-768.

Hyndman, R. J., & Koehler, A. B. (2006). Another look at measures of forecast accuracy. *International journal of forecasting*, *22*(4), 679-688.

Jackson, M. D., Blundy, J., & Sparks, R. S. J. (2018). Chemical differentiation, cold storage and remobilization of magma in the Earth's crust. *Nature*, *564*(7736), 405-409.

Jagoutz, O. (2014). Arc crustal differentiation mechanisms. *Earth and Planetary Science Letters*, *396*, 267-277.

Jia, Y., & Ma, J. (2017). What can machine learning do for seismic data processing? An interpolation application. *Geophysics*, *82*(3), V163-V177.

Kelley, D. F., & Barton, M. (2008). Pressures of crystallization of Icelandic magmas. *Journal of Petrology*, *49*(3), 465-492.

Kern, J. M., de Silva, S. L., Schmitt, A. K., Kaiser, J. F., Iriarte, A. R., & Economos, R. (2016). Geochronological imaging of an episodically constructed subvolcanic batholith: U-Pb in zircon chronochemistry of the Altiplano-Puna Volcanic Complex of the Central Andes. *Geosphere*, *12*(4), 1054-1077.

Kiser, E., Palomeras, I., Levander, A., Zelt, C., Harder, S., Schmandt, B., ... & Ulberg, C. (2016). Magma reservoirs from the upper crust to the Moho inferred from high-resolution Vp and Vs models beneath Mount St. Helens, Washington State, USA. *Geology*, *44*(6), 411-414.

Kuritani, T., Yokoyama, T., Kitagawa, H., Kobayashi, K., & Nakamura, E. (2011). Geochemical evolution of historical lavas from Askja Volcano, Iceland: implications for mechanisms and timescales of magmatic differentiation. *Geochimica et Cosmochimica Acta*, *75*(2), 570-587.

Lee, C. T. A., & Bachmann, O. (2014). How important is the role of crystal fractionation in making intermediate magmas? Insights from Zr and P systematics. *Earth and Planetary Science Letters*, *393*, 266-274.

Le Maitre, R. W., Streckeisen, A., Zanettin, B., Le Bas, M. J., Bonin, B., Bateman, P., ... & Woolley, A. R. (2002). Igneous rocks. *A Classification and Glossary of Terms: Recommendations of the International Union of Geological Sciences Subcommission on the Systematics of Igneous Rocks, Cambridge University Press, Cambridge*, *2*.

Lees, J. M. (1992). The magma system of Mount St. Helens: Non-linear high-resolution P-wave tomography. *Journal of volcanology and geothermal research*, *53*(1-4), 103-116.

Lindsay, J. M., Schmitt, A. K., Trumbull, R. B., De Silva, S. L., Siebel, W., & Emmermann, R. (2001). Magmatic evolution of the La Pacana caldera system, Central Andes, Chile: Compositional variation of two cogenetic, large-volume felsic ignimbrites. *Journal of Petrology*, *42*(3), 459-486.

Lindsay, J. M., De Silva, S., Trumbull, R., Emmermann, R., & Wemmer, K. (2001). La Pacana caldera, N. Chile: a re-evaluation of the stratigraphy and volcanology of one of the world's largest resurgent calderas. *Journal of Volcanology and Geothermal Research*, *106*(1-2), 145-173.

Lissenberg, C. J., MacLeod, C. J., & Bennett, E. N. (2019). Consequences of a crystal mush-dominated magma plumbing system: a mid-ocean ridge perspective. *Philosophical Transactions of the Royal Society A*, *377*(2139), 20180014.

Maclennan, J. (2019). Mafic tiers and transient mushes: evidence from Iceland. *Philosophical Transactions of the Royal Society A*, *377*(2139), 20180021.

Magee, C., Stevenson, C. T., Ebmeier, S. K., Keir, D., Hammond, J. O., Gottsmann, J. H., ... & Jackson, M. D. (2018). Magma plumbing systems: a geophysical perspective. *Journal of Petrology*, *59*(6), 1217-1251.

Masotta, M., Mollo, S., Gaeta, M., & Freda, C. (2016). Melt extraction in mush zones: The case of crystal-rich enclaves at the Sabatini Volcanic District (central Italy). *Lithos*, *248*, 288-292.

Melson, W. G. (1983). Monitoring the 1980-1982 eruptions of Mount St. Helens: compositions and abundances of glass. *Science*, *221*(4618), 1387-1391.

Merzbacher, C., & Eggler, D. H. (1984). A magmatic geohygrometer: application to Mount St. Helens and other dacitic magmas. *Geology*, *12*(10), 587-590.

Mohammed, M., Khan, M. B., & Bashier, E. B. M. (2016). *Machine learning: algorithms and applications*. Crc Press.

Mollo, S., Del Gaudio, P., Ventura, G., Iezzi, G., & Scarlato, P. (2010). Dependence of clinopyroxene composition on cooling rate in basaltic magmas: Implications for thermobarometry. *Lithos*, *118*(3-4), 302-312.

Montierth, C., Johnston, A. D., & Cashman, K. V. (1995). An empirical glass-composition-based geothermometer for Mauna Loa lavas. *Washington DC American Geophysical Union Geophysical Monograph Series*, *92*, 207-217.

Mutch, E. J. F., Blundy, J. D., Tattitch, B. C., Cooper, F. J., & Brooker, R. A. (2016). An experimental study of amphibole stability in low-pressure granitic magmas and a revised Al-in-hornblende geobarometer. *Contributions to Mineralogy and Petrology*, *171*, 1-27.

Nazzareni, S., Rossi, S., Petrelli, M., & Caricchi, L. (2020). Architecture of the magmatic system in the Main Ethiopian Rift. *Dynamic Magma Evolution*, 133-151.

Neave, D. A., & Putirka, K. D. (2017). A new clinopyroxene-liquid barometer, and implications for magma storage pressures under Icelandic rift zones. *American Mineralogist*, *102*(4), 777-794.

Nichols, M. L., Malone, S. D., Moran, S. C., Thelen, W. A., & Vidale, J. E. (2011). Deep long-period earthquakes beneath Washington and Oregon volcanoes. *Journal of Volcanology and Geothermal Research*, *200*(3-4), 116-128.

Petrone, C. M., Bugatti, G., Braschi, E., & Tommasini, S. (2016). Pre-eruptive magmatic processes re-timed using a non-isothermal approach to magma chamber dynamics. *Nature communications*, *7*(1), 12946.

Plank, T., & Forsyth, D. W. (2016). Thermal structure and melting conditions in the mantle beneath the Basin and Range province from seismology and petrology. *Geochemistry, Geophysics, Geosystems*, *17*(4), 1312-1338.

Popa, R. G., Bachmann, O., & Huber, C. (2021). Explosive or effusive style of volcanic eruption determined by magma storage conditions. *Nature Geoscience*, *14*(10), 781-786.

Pritchard, M. E., De Silva, S. L., Michelfelder, G., Zandt, G., McNutt, S. R., Gottsmann, J., ... & Ward, K. M. (2018). Synthesis: PLUTONS: Investigating the relationship between pluton growth and volcanism in the Central Andes. *Geosphere*, *14*(3), 954-982.

Putirka, K. D. (2008). Thermometers and barometers for volcanic systems. *Reviews in mineralogy and geochemistry*, *69*(1), 61-120.

Putirka, K. (2016). Amphibole thermometers and barometers for igneous systems and some implications for eruption mechanisms of felsic magmas at arc volcanoes. *American Mineralogist*, *101*(4), 841-858.

Putirka, K. D. (2017). Down the crater: where magmas are stored and why they erupt. *Elements*, *13*(1), 11-16.

R Core Team, R. (2013). R: A language and environment for statistical computing.

Rutherford, M. J., & Devine, J. D. (1988). The May 18, 1980, eruption of Mount St. Helens: 3. Stability and chemistry of amphibole in the magma chamber. *Journal of Geophysical Research: Solid Earth*, *93*(B10), 11949-11959.

Rutherford, M. J., Sigurdsson, H., Carey, S., & Davis, A. (1985). The May 18, 1980, eruption of Mount St. Helens: 1. Melt composition and experimental phase equilibria. *Journal of Geophysical Research: Solid Earth*, *90*(B4), 2929-2947.

Ruprecht, P., & Bachmann, O. (2010). Pre-eruptive reheating during magma mixing at Quizapu volcano and the implications for the explosiveness of silicic arc volcanoes. *Geology*, *38*(10), 919-922.

Ruprecht, P., & Wörner, G. (2007). Variable regimes in magma systems documented in plagioclase zoning patterns: El Misti stratovolcano and Andahua monogenetic cones. *Journal of Volcanology and Geothermal Research*, *165*(3-4), 142-162.

Salisbury, M. J., Jicha, B. R., de Silva, S. L., Singer, B. S., Jiménez, N. C., & Ort, M. H. (2011). 40Ar/39Ar chronostratigraphy of Altiplano-Puna volcanic complex ignimbrites reveals the development of a major magmatic province. *Bulletin*, *123*(5-6), 821-840.

Schattel, N., Portnyagin, M., Golowin, R., Hoernle, K., & Bindeman, I. (2014). Contrasting conditions of rift and off-rift silicic magma origin on Iceland. *Geophysical Research Letters*, *41*(16), 5813-5820.

Schmitt, A., De Silva, S., Trumbull, R., & Emmermann, R. (2001). Magma evolution in the Purico ignimbrite complex, northern Chile: evidence for zoning of a dacitic magma by injection of rhyolitic melts following mafic recharge. *Contributions to Mineralogy and Petrology*, *140*, 680-700.

Seropian, G., Rust, A. C., & Sparks, R. S. J. (2018). The gravitational stability of lenses in magma mushes: Confined Rayleigh-Taylor instabilities. *Journal of Geophysical Research: Solid Earth*, *123*(5), 3593-3607.

Smith, D. R., & Leeman, W. P. (1987). Petrogenesis of Mount St. Helens dacitic magmas. *Journal of Geophysical Research: Solid Earth*, *92*(B10), 10313-10334.

Sparks, R. S. J., Annen, C., Blundy, J. D., Cashman, K. V., Rust, A. C., & Jackson, M. D. (2019). Formation and dynamics of magma reservoirs. *Philosophical Transactions of the Royal society A*, *377*(2139), 20180019.

Sparks, R. S. J., & Marshall, L. A. (1986). Thermal and mechanical constraints on mixing between mafic and silicic magmas. *Journal of volcanology and Geothermal Research*, *29*(1-4), 99-124.

Thomson, A. R., Kohn, S. C., Prabhu, A., & Walter, M. J. (2021). Evaluating the formation pressure of diamond-hosted majoritic garnets: A machine learning majorite barometer. *Journal of Geophysical Research: Solid Earth*, *126*(3), e2020JB020604.

Thornber, C. R., Heliker, C., Sherrod, D. R., Kauahikaua, J. P., Miklius, A., Okubo, P. G., ... & Meeker, G. P. (2003). Kilauea east rift zone magmatism: An episode 54 perspective. *Journal of Petrology*, *44*(9), 1525-1559.

Tibaldi, A. M., Otamendi, J. E., Cristofolini, E. A., Baliani, I., Walker Jr, B. A., & Bergantz, G. W. (2013). Reconstruction of the Early Ordovician Famatinian arc through thermobarometry in lower and middle crustal exposures, Sierra de Valle Fértil, Argentina. *Tectonophysics*, *589*, 151-166.

Till, C. B. (2017). A review and update of mantle thermobarometry for primitive arc magmas. *American Mineralogist*, *102*(5), 931-947.

Waters, L. E., & Lange, R. A. (2015). An updated calibration of the plagioclase-liquid hygrometer-thermometer applicable to basalts through rhyolites. *American mineralogist*, *100*(10), 2172-2184.

Ubide, T., & Kamber, B. S. (2018). Volcanic crystals as time capsules of eruption history. *Nature communications*, *9*(1), 326.

Ulberg, C. W., Creager, K. C., Moran, S. C., Abers, G. A., Thelen, W. A., Levander, A., ... & Crosson, R. S. (2020). Local source Vp and Vs tomography in the Mount St. Helens region with the iMUSH broadband array. *Geochemistry, Geophysics, Geosystems*, *21*(3), e2019GC008888.

Van Zalinge, M. E., Mark, D. F., Sparks, R. S. J., Tremblay, M. M., Keller, C. B., Cooper, F. J., & Rust, A. (2022). Timescales for pluton growth, magma-chamber formation and super-eruptions. *Nature*, *608*(7921), 87-92.

Wanke, M., Clynne, M. A., von Quadt, A., Vennemann, T. W., & Bachmann, O. (2019). Geochemical and petrological diversity of mafic magmas from Mount St. Helens. *Contributions to Mineralogy and Petrology*, *174*, 1-25.

Ward, K. M., Delph, J. R., Zandt, G., Beck, S. L., & Ducea, M. N. (2017). Magmatic evolution of a Cordilleran flare-up and its role in the creation of silicic crust. *Scientific reports*, *7*(1), 9047.

Weber, G., Blundy, J., & Bevan, D., (2023) Mush amalgamation, short residence, and sparse detectability of eruptible magma before Andean super-eruptions. *Geochemistry, Geophysics, Geosystems*, doi: 10.1029/2022GC010732
Weber, G., Arce, J. L., Ulianov, A., & Caricchi, L. (2019). A recurrent magmatic pattern on observable timescales prior to plinian eruptions from Nevado de Toluca (Mexico). *Journal of Geophysical Research: Solid Earth*, *124*(11), 10999-11021.

Weber, G., & Castro, J. M. (2017). Phase petrology reveals shallow magma storage prior to large explosive silicic eruptions at Hekla volcano, Iceland. *Earth and Planetary Science Letters*, *466*, 168-180.

Wieser, P. E., Kent, A. J., Till, C. B., Donovan, J., Neave, D. A., Blatter, D. L., & Krawczynski, M. J. (2023). Barometers Behaving Badly I: Assessing the Influence of Analytical and Experimental Uncertainty on Clinopyroxene Thermobarometry Calculations at Crustal Conditions. *Journal of Petrology*, *64*(2), egac126.

Wright, M., Ziegler, A. (2017). ranger: A Fast Implementation of Random Forests for High Dimensional Data in C++ and R. Journal of Statistical Software, 77(1), 1-17. doi:10.18637/jss.v077.i01

Yang, H. J., Kinzler, R. J., & Grove, T. L. (1996). Experiments and models of anhydrous, basaltic olivine-plagioclase-augite saturated melts from 0.001 to 10 kbar. *Contributions to Mineralogy and Petrology*, *124*(1), 1-18.

Zhou, Z. H. (2021). *Machine learning*. Springer Nature.

Ziberna, L., Green, E. C., & Blundy, J. D. (2017). Multiple-reaction geobarometry for olivine-bearing igneous rocks. *American Mineralogist: Journal of Earth and Planetary Materials*, *102*(12), 2349-2366.